

Multiple morphogens and rapid elongation promote segmental patterning during development

Yuchi Qiu₀^{1¤}, Lianna Fung₀^{2,3}, Thomas F. Schilling^{2,3}*, Qing Nie₀^{1,2,3}*

- 1 Department of Mathematics, University of California, Irvine, California, United States of America,
- 2 Department of Developmental and Cell Biology, University of California, Irvine, California, United States of America, 3 The NSF-Simons Center for Multiscale Cell Fate Research, University of California, Irvine, California, United States of America
- Eurrent address: Department of Mathematics, Michigan State University, Michigan, United States of America
- * tshilli@uci.edu (TFS); qnie@math.uci.edu (QN)



OPEN ACCESS

Citation: Qiu Y, Fung L, Schilling TF, Nie Q (2021) Multiple morphogens and rapid elongation promote segmental patterning during development. PLoS Comput Biol 17(6): e1009077. https://doi.org/10.1371/journal.pcbi.1009077

Editor: David Umulis, Purdue University, UNITED STATES

Received: December 1, 2020

Accepted: May 13, 2021

Published: June 23, 2021

Copyright: © 2021 Qiu et al. This is an open access article distributed under the terms of the Creative Commons Attribution License, which permits unrestricted use, distribution, and reproduction in any medium, provided the original author and source are credited.

Data Availability Statement: All relevant data are within the manuscript and its Supporting Information files.

Funding: TFS was supported by National Science Foundation grant MCB2028424, and National Institutes of Health grants DE013828 and AR067797. QN was supported by a National Science Foundation grant DMS1763272, a National Institutes of Health grant U01AR073159, and a grant from the Simons Foundation 594598. The funders had no role in study design, data collection

Abstract

The vertebrate hindbrain is segmented into rhombomeres (r) initially defined by distinct domains of gene expression. Previous studies have shown that noise-induced gene regulation and cell sorting are critical for the sharpening of rhombomere boundaries, which start out rough in the forming neural plate (NP) and sharpen over time. However, the mechanisms controlling simultaneous formation of multiple rhombomeres and accuracy in their sizes are unclear. We have developed a stochastic multiscale cell-based model that explicitly incorporates dynamic morphogenetic changes (i.e. convergent-extension of the NP), multiple morphogens, and gene regulatory networks to investigate the formation of rhombomeres and their corresponding boundaries in the zebrafish hindbrain. During pattern initiation, the short-range signal, fibroblast growth factor (FGF), works together with the longerrange morphogen, retinoic acid (RA), to specify all of these boundaries and maintain accurately sized segments with sharp boundaries. At later stages of patterning, we show a nonlinear change in the shape of rhombomeres with rapid left-right narrowing of the NP followed by slower dynamics. Rapid initial convergence improves boundary sharpness and segment size by regulating cell sorting and cell fate both independently and coordinately. Overall, multiple morphogens and tissue dynamics synergize to regulate the sizes and boundaries of multiple segments during development.

Author summary

In segmental pattern formation, chemical gradients control gene expression in a concentration-dependent manner to specify distinct gene expression domains. Despite the stochasticity inherent to such biological processes, precise and accurate borders form between segmental gene expression domains. Previous work has revealed synergy between gene regulation and cell sorting in sharpening borders that are initially rough. However, it is still poorly understood how size and boundary sharpness of *multiple* segments are

and analysis, decision to publish, or preparation of the manuscript.

Competing interests: The authors have declared that no competing interests exist.

regulated in a tissue that changes dramatically in its morphology as the embryo develops. Here we develop a stochastic multiscale cell-base model to investigate these questions. Two novel strategies synergize to promote accurate segment formation, a combination of long- and short-range morphogens plus rapid tissue convergence, with one responsible for pattern initiation and the other enabling pattern refinement.

Introduction

A fundamental question in developmental biology is how cell fate decisions are coordinated with tissue morphogenetic changes during pattern formation. During embryogenesis, cells must convert concentration-dependent positional information from diffusible chemical morphogens into coordinated cell fate decisions [1–3]. Mathematical models have successfully integrated tissue morphogenesis and spatial signaling during patterning of embryonic segments in both flies [4,5] and vertebrates [6–8], in structures such as the wing imaginal discs in *Drosophila* [9–11], as well as the limb buds [12], neural tube [13–15], hindbrain [16–18], pharyngeal arches [19], skin [20,21] and hair follicles [22] of vertebrates.

Understanding stochastic effects in patterning systems, particularly how precision is achieved in spite of biological noise in gene expression and spatial signals, is a major challenge in developmental biology. Noise attenuation mechanisms in gene expression have been widely explored in diverse cellular networks [23,24]. For spatial signals, binding with membrane-bound non-signaling entities [25], regulation of gradient steepness by ligand shuttling [26,27] and self-regulated ligand uptake [28,29] can reduce spatial variation in morphogen gradients. Anti-parallel morphogens [14] and gene regulatory networks [30–32] that translate noisy spatial signals into cell fate decisions can also reduce patterning errors. Interestingly, noise in gene expression can counteract other stochastic effects (e.g. noise in morphogen levels) to improve pattern formation precision [17,33]. In addition to these molecular strategies, pattern precision can be improved through cellular strategies, such as cell sorting driven by cell-cell interactions [16,20] or "community effects" of signals from adjacent cells [34]. Previous modeling studies have often neglected to take into account rapid changes in tissue morphology, and how the interaction between these and noise attenuation mechanisms impacts pattern precision remains poorly understood.

The embryonic zebrafish hindbrain is a powerful model system to study the roles of gene regulation, stochasticity, cell sorting, and tissue morphogenesis in segmental pattern formation. Neurons in the hindbrain contribute to the cranial nerves that innervate the face and neck and control many involuntary functions, such as feeding and breathing. These neurons arise in early embryonic segments, called rhombomeres (r), that progressively subdivide along the anterior-posterior (A-P) axis [35]. Initial gene expression domains that specify segmental cell identities in rhombomeres 1-7 (r1-7) have rough borders that subsequently sharpen [17,36]. Several spatial signals provide positional information for the establishment of rhombomeres, such as retinoic acid (RA) [28,37-40] and fibroblast growth factors (FGFs) [41-45]. These signals regulate numerous transcription factors, including hox genes, krox20, val, vhnf1 and irx, with rhombomere-specific expression domains that specify rhombomere cell identity [46–48]. Rhombomere-specific gene regulatory networks commit cells to distinct segmental fates and can switch their identities from one segment to another by interpreting RA and FGF signals [34,49]. In addition, the complementary segmental expression of Ephrins and Eph receptors drives boundary sharpening by regulating cell sorting with differential adhesion/ repulsion [50-53]. Previous computational models incorporating one morphogen, RA, and two transcription factors, hoxb1a and krox20, successfully mimic boundary sharpening in r3-5



by incorporating gene regulation and cell sorting [16,17]. During the period when these boundaries sharpen, the hindbrain grows and elongates, particularly, the hindbrain narrows along the left-right (L-R) axis and elongates along the anterior-posterior (A-P) axis, which is often termed convergent-extension [49,54]. However, previous computational models have shown that tissue elongation disrupts the sharpening of rhombomere boundaries [17]. It remains unclear in any segmented tissue how multiple segments simultaneously form with accurate sizes and sharp boundaries during such morphogenetic tissue dynamics.

Here we consider hindbrain patterning across multiple stages, from pattern initiation to sharpening, across multiple segments (r2-6) and in the context of morphogenetic changes in hindbrain size and shape. We include a second morphogen in our model, FGF produced in r4, and two additional transcription factors, *vhnf1* and *irx3*. We find that FGF produced in r4 is critical to specify the r5/r6 boundary, and to achieve a robust five-segment pattern with accurate segment sizes and sharp boundaries despite variations in initial gene expression. At later stages of patterning, we show experimentally that L-R narrowing of the zebrafish hindbrain occurs rapidly at first (11–12 hours post fertilization (hpf)), but the narrowing rate drops rapidly over the following two hours (12–14 hpf). Interestingly, comparisons of hindbrain pattern formation in our model under different convergence rates suggest that such a rapid initial convergence facilitates robust patterning, both in the accuracy of segment size and boundary sharpness. This rapid initial convergence helps mediate a trade-off between boundary sharpness and segment size. Together, the cooperation between two morphogens and morphogenetic dynamics effectively regulates robust segmental patterning in the zebrafish hindbrain.

Results

A stochastic multiscale cell-based model for hindbrain segmentation

To address how multiple morphogens and dynamics of tissue morphogenesis contribute to segmental pattern formation in the hindbrain, we developed a computational model that incorporates stochastic gene regulation, cell sorting and tissue shape changes (Fig 1). We first provide an overview of the elements, assumptions, and metrics included in our models (details see Methods and S1 Text).

Hindbrain morphogenesis and computational domains. During embryogenesis from 11–14 hpf, the zebrafish hindbrain narrows along the L-R axis and elongates along the A-P axis [49,54]. The midbrain-hindbrain boundary (MHB) (anterior to the hindbrain and adjacent to r1) and the RA production region (posterior to the hindbrain and adjacent to r7) provide A-P landmarks for the region that forms the hindbrain (Fig 1A). To quantify these changes in size and shape, we performed whole mount in situ hybridization with markers for the MHB (otx2), r3 and r5 (krox20) and RA production (aldh1a2). At each hour between 11–14 hpf, we measured hindbrain width at the level of r4 as well as the A-P distance between the otx2 and aldh1a2 domains (Fig 2A and 2B). Based on these experimental measurements, we modeled the hindbrain (r1-r7) along with the RA production region as a rectangle, subsequently referred to as the morphogen domain (Fig 1B). Two morphogens, RA and FGF, were modeled in the morphogen domain. Due to the expensive computational cost, instead of modeling all cells in the morphogen domain for this study, we explicitly modeled cells in a smaller region containing r2-r6, subsequently referred to as the tissue domain.

Morphogens, gene regulation and cell fate. Gene expression in the zebrafish hindbrain initially forms a rough r2-6 pattern at 11 hpf, which is refined over time into five precise segments of similar size with four sharp boundaries by 14 hpf (Fig 1C and 1D). RA synthesized in somites adjacent to the anterior spinal cord diffuses anteriorly and is required for proper rhombomere formation, including direct activation of *vhnf1* in r5 and r6 and *hoxb1a* in r4

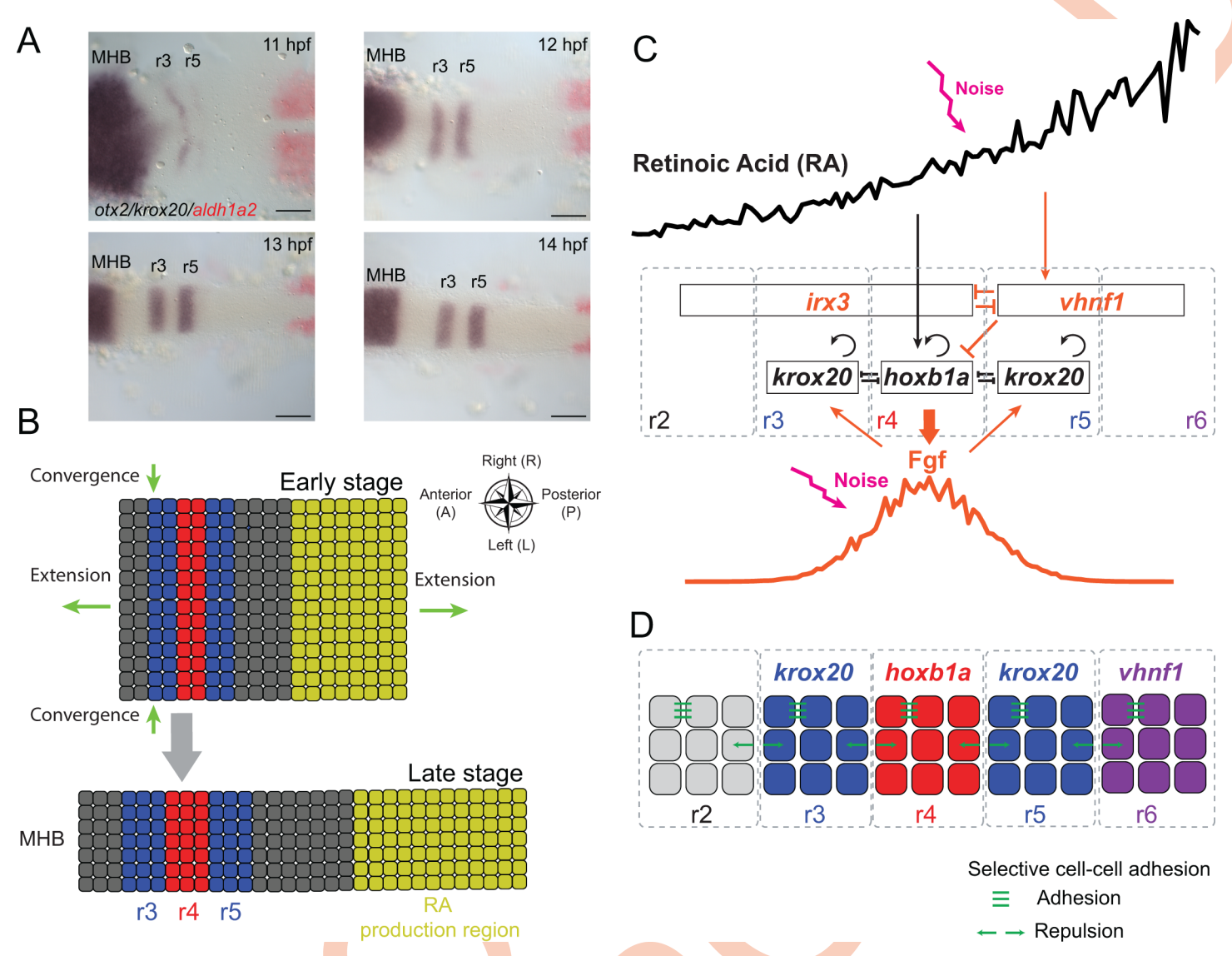
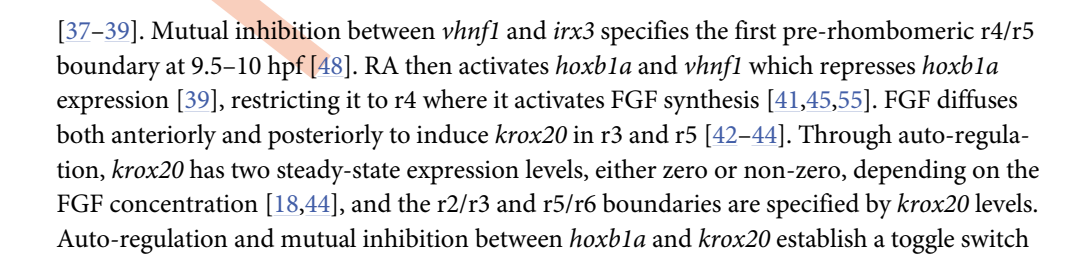


Fig 1. Model schematic and zebrafish hindbrain morphology. (A) Two-color whole mount in situ hybridization of embryonic zebrafish hindbrains for *otx2* (purple, anterior region, far left), *krox20* (purple segments, center) and *aldh1a2* (red, far right) transcripts from 11 to 14 hpf. *otx2* marks the midbrain-hindbrain boundary (MHB), *krox20* marks r3 and r5 and *aldh1a2* marks the RA production region. Embryos are flat-mounted and shown in dorsal view with anterior to the left. Scale bars: 100 µm.

(B) Illustration depicting convergent-extension of the hindbrain. The entire rectangular region, including r1-7 and the RA production region, constitutes the morphogen domain. The hindbrain narrows in the L-R direction (width) and elongates in the A-P direction. (C) Gene regulatory network used to model hindbrain patterning in r2-6. Genes and morphogens with black font were previously used for modeling the r3-r5 pattern [17], while additional factors considered in this model are shown in orange font. Pointed arrows depict up-regulation/activation and blunt arrows depict down-regulation/inhibition. Two morphogens, retinoic acid (RA) and Fibroblast Growth Factor (FGF) diffuse and form two distinct gradients to govern downstream gene expression. (D) Illustration depicting r2-6 and distinct identities (i.e. gene expression signatures) underlying selective cell sorting. Cells in r3 and r5 (blue) express *krox20* and cells in r4 (red) express *hoxb1a*, while both *krox20* and *hoxb1a* levels are low in r2 and r6. Cells in r6 (purple) have high *vhnf1* expression. Cells with the same segmental identity attract each other and cells with different identities repulse each other.



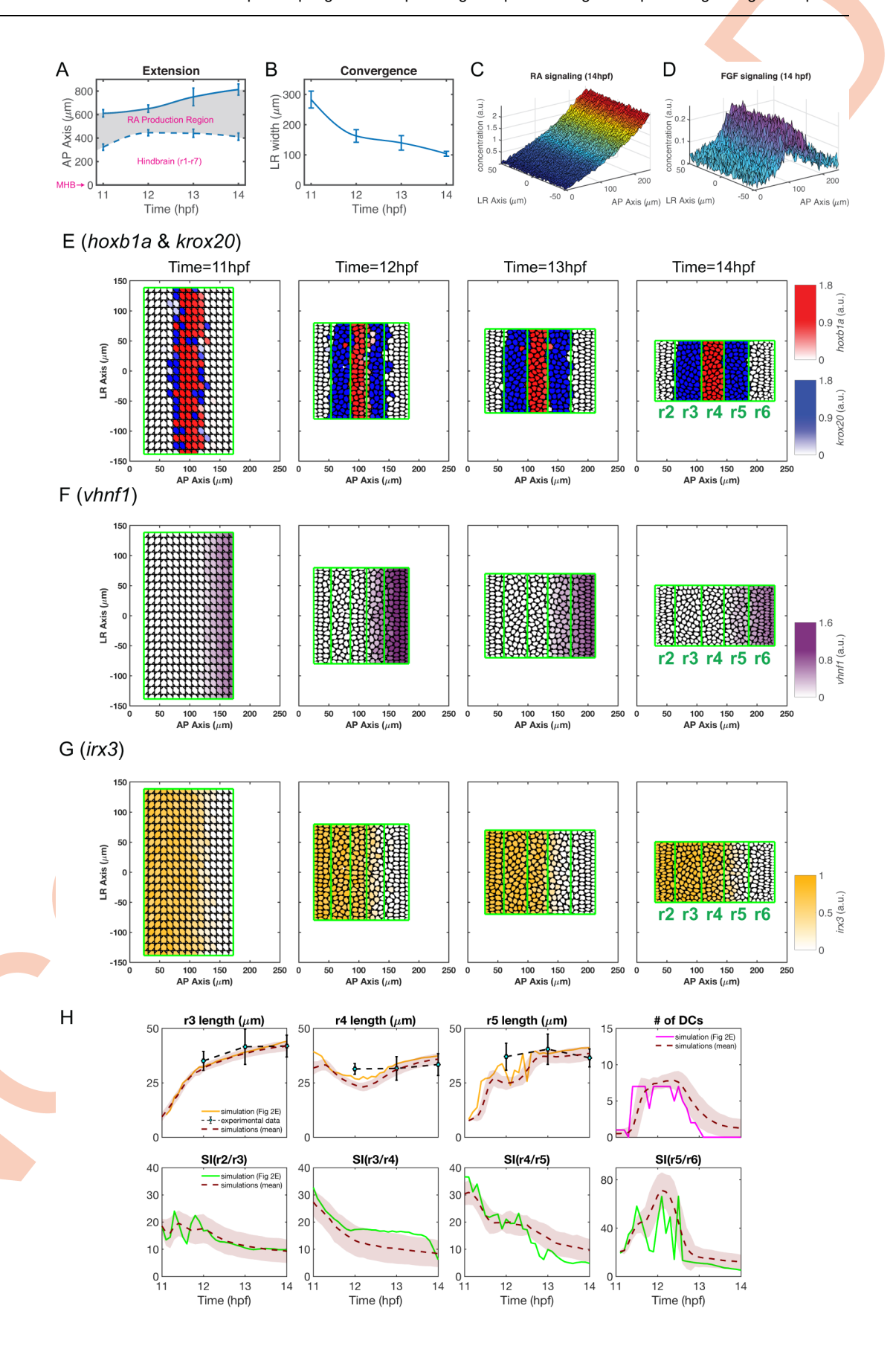


Fig 2. A baseline simulation mimics rhombomere boundary sharpening. (A,B) Experimental measurements of hindbrain dimensions along the A-P (A) and L-R (B) axes at 11, 12, 13 and 14 hpf. Error bars represent standard deviation. Cubic interpolation is used to obtain the smooth curves used in the model. (A) A-P hindbrain length was measured from the posterior edge of the mid-hindbrain boundary (MHB) to the anterior edge of the RA production region. A-P length of the RA production region was based on measurements of the *aldh1a2* expression domain. (B) L-R hindbrain width was measured at the A-P position of r4. (C,D) Predicted noisy distributions of morphogen signaling at 14 hpf (C) RA ([RA]_{in}). (D) FGF ([FGF]_{signal}). (E-G) Time series of gene expression in r2-6 (the hindbrain is represented as a rectangle for simplification): (E) *hoxb1a* (red) and *krox20* (blue), (F) *vhnf1* (purple), (G) *irx3* (yellow). (H) Quantifications of rhombomere length, number of dislocated cells (DCs) and sharpness indices (SIs) versus time. Rhombomere lengths (r3-5), and SIs for four boundaries (SI(r2/r3), SI(r3/r4), SI(r4/r5), SI(r5/r6)) and DC number in multiple simulations (n = 100): 'solid line': quantities for the simulation shown in (E); 'brown dashed line' indicates the average and the width of 'brown shade" indicates standard deviation; 'black dashed line' represents rhombomere lengths from experimental measurements and the error bars represent standard deviation.

that specifies and refines the r3/r4 and r4/r5 boundaries [17]. As a result, three distinct cell fates are specified by *hoxb1a* and *krox20* expression levels to establish the r2-r6 pattern, specifically, high *hoxb1a* and low *krox20* expression in r4, low *hoxb1a* and high *krox20* expression in r3 and r5, and low expression of both *hoxb1a* and *krox20* in r2 and r6 (Fig 1D).

In the model, morphogens (RA and FGF) were described by stochastic PDEs in a continuum fashion. Regulation of genes downstream of morphogens was modeled using stochastic ODEs for each individual cell. Interactions between morphogens were modeled at a regular rectangular mesh in the morphogen domain, and the downstream genes for each cell were modeled as being located at the center of each individual cell. Numerical interpolation was used to capture the interplay between morphogens and gene regulation modeled at different grid points (Section 1 in S1 Text).

Mechanical models for individual cells. In the cell mechanical model, we used the subcellular element method (SCEM) [16,56] to model individual cells and cell-cell mechanical interactions involved in cell sorting (Section 2 in S1 Text). In this computational formalism, an individual cell consists of a constant number of sub-cellular elements (i.e. nodes). Elements interact according to a prescribed force potential. This force between elements within the same cell is repulsive at short ranges and attractive at long ranges to maintain stable cell volume and circular structure. The forces between elements from different cells are repulsive at short ranges to prevent cell overlaps. At longer ranges, the intercellular forces between elements can be either repulsive or attractive depending on cell identities.

Cell sorting. In the zebrafish hindbrain, cell sorting has selectivity based on cell identities. One well-known mechanism of selectivity is cell-cell adhesion mediated by Ephrin-Eph signaling. Ephrin-B2 ligands are expressed highly in even-numbered rhombomeres (r2, r4 and r6), while EphA4 receptors are expressed highly in odd-numbered rhombomeres (r3 and r5), and this alternating pattern controls repulsion between cells in one rhombomere and another [52]. Depletion of EphA4 has more dramatic effects on rhombomere boundaries than EphrinB2a, but knockdown of both enhances boundary defects [50]. Krox20 directly activates transcription of *ephA4* [57], thereby regulating Ephrin-Eph mediated cell sorting. Our model mimics the selective cell-cell adhesion between two cells based on their *krox20* expression levels (Fig 1D). Specifically, cells attract each other if they have similar *krox20* levels, and repel each other if one expresses *krox20* and the other does not.

Initial conditions. We chose 11 hpf as the starting point for our modeling study soon after the initiation of gene expression in some rhombomeres. At this stage in the simulations cells were assumed to align uniformly in the rectangular tissue domain. For initial gene expression, we first ran simulations with the stochastic gene regulation model over two simulated hours prior to 11 hpf and used those simulation results as the initial condition at 11hpf. We started with equilibrium solution for RA by solving the corresponding steady-state PDE



because RA gradients are established as early as 6 hpf [39]. Because *vhnf1* and *irx3* expression appear much earlier than *hoxb1a*, *krox20* and FGF [39], we ran stochastic simulations for RA, *vhnf1* and *irx3* in the first hour with zero values for *vhnf1* and *irx3*. In the second hour, we included stochastic simulations for all morphogens and genes. *krox20* and FGF start with zero expression while *hoxb1a* starts with a constant expression level because *hoxb1a* has weak expression over the hindbrain domain at early stages [17] and shows dynamic changes in expression earlier than FGF or *krox20* [48].

One-dimensional gene expression model. In the one-dimensional gene expression models, we consider steady-state solutions of genes and morphogens in a one-dimensional fixed A-P domain (Section 3 in S1 Text). The initial conditions were chosen similarly to the full model. Equilibrium solutions for RA, *vhnf1* and *irx3* were taken as the initial conditions. Both *krox20* and FGF levels were initially set at zero. We included *hoxb1a* expression at low but non-zero initial levels.

A cell sorting-only model. In the model with only cell sorting without gene regulation, cells sorted based on their pre-assigned identities, and cell identities and numbers did not change throughout the simulations. The initial "salt-and-pepper" pattern of cell identities was sampled by a mixture Gaussian probability distribution based on each cell's A-P position (Section 4 in S1 Text).

Quantification of cell fate, rhombomere boundary A-P locations and boundary sharpness. Three cell identities based on threshold levels of high or low expression of *hoxb1a* and *krox20* in the five segments (r2-6) were considered. Once these three cell identities were determined in r2-r6 we evaluated rhombomere boundaries (Section 5 in S1 Text). We defined three critical quantities in our simulations: boundary location along the A-P axis, boundary sharpness (represented as a sharpness index, SI) and the number of dislocated cells (DCs) (see Methods). Four boundaries between rhombomeres (r2/r3, r3/r4, r4/r5 and r5/r6) are all perpendicular to the A-P axis. For a single boundary determination, we selected a predefined boundary and calculated total deviations of cells located on the wrong side of this predefined boundary. The total deviations were minimized over the A-P position of the predefined boundary. SI was defined by the minima of total deviations and the A-P position of this boundary was defined based on these minima. A lower SI indicates a sharper boundary. DCs are cells located over three cell-diameters away from the rhombomere to which they belong and they are excluded in calculating boundary location. If the number of DCs exceeds 8 cells, we consider the pattern failed.

Including multiple morphogens and tissue morphogenesis in the models recapitulates the r2-6 pattern

The stochastic multiscale cell-based model successfully recapitulated the dynamics of r2-6 formation observed in the zebrafish hindbrain. As shown for one stochastic simulation with spatial distributions of multiple genes, both RA and FGF signals have noisy distributions over the space (Fig 2C and 2D). The RA gradient decreases from its origins at the posterior end of the hindbrain to the anterior, while FGF levels are high in r4 where it is secreted and decreases in both anterior and posterior directions. By generating a time series of the spatial patterns of gene expression (Fig 2E-2G), including hoxb1a, krox20, vhnf1 and irx3, our model recapitulates rhombomere boundary sharpening [17,49]. For example, krox20 is weakly expressed in r3 and r5 at 11 hpf and upregulated by 12 hpf, with expression stronger in r3 than r5 (Figs 1A and 2E). At this stage, hoxb1a+ and krox20+ cells intermingle and a few cells close to the r4/r5 boundary undergo identity switching as they co-express low levels of both krox20 and hoxb1a [49]. By 13 hpf, cells closer to the boundaries and most of the krox20/hoxb1a co-expressing cells commit to one segment or another and boundaries become sharper. At 14 hpf, all cells



segregate to their territories and the boundaries fully sharpen, producing a precise five-segment pattern.

The modeling output naturally accounts for the sharpening of other gene expression boundaries in r2-6, despite differences in their interactions. For example, the anterior edge of *vhnf1* expression and the posterior edge of *irx3* expression specify the position of the prerhombomeric r4/r5 boundary at 11 hpf (Fig 2F and 2G). At later stages, this vhnf1/irx3 border shifts posteriorly to become located in r5 [48]. Unlike hoxb1a and krox20, vhnf1 does not autoinduce itself to maintain its own expression without RA signals. Consequently, *vhnf1* shifts posteriorly [39] after 12 hpf as RA decreases everywhere (S1C Fig).

Stochastic simulations were repeated independently (Fig 2H). The results are consistent with experimental measurements of rhombomere A-P length at 14 hpf ($r3 = 42\pm5 \mu m$, $r4 = 34\pm5 \mu m$, $r5 = 37 \pm 4 \mu m$) as well as sharpening. For example, from 11–12 hpf, identity switching affects the sharpness of the r4/r5 boundary [17], with a higher SI and DC number during this period. From 12-14 hpf, SI and DC number gradually decrease to the minimum as all boundaries sharpen.

Cooperation between RA and FGF improves robustness of initiation of the segmental pattern

A previous model that only considered the RA morphogen gradient without cell sorting or convergent extension successfully simulated many aspects of the formation of the r2-5 pattern [17]. In the model, hoxbla and krox20 were considered as direct downstream targets of RA, despite krox20 being indirectly induced by RA through hoxb1a and FGF. Our new model incorporates both RA and FGF as well as these additional features of krox20 regulation.

Comparing the two-morphogen (RA + FGF) to the one-morphogen (RA) model reveals many similarities and some key differences (Fig 3). In both, the borders between hoxb1a and krox20 specify r3/r4 and r4/r5 boundaries, the border between vhnf1 and irx3 lies posterior to the r4/r5 boundary, and krox20 has two steady-state levels induced by either RA (one-morphogen model) or FGF (two-morphogen model) depending on the morphogen levels. In the two-morphogen model, FGF has the highest expression in r4 where it is secreted and decreases in both anterior and posterior directions. By inducing *krox20* in a concentration-dependent manner, FGF can specify the r2/r3 and r5/r6 boundaries. In contrast, the one-morphogen model, with RA decreasing monotonically from posterior to anterior, can only specify r2/r3 and not the r5/r6 boundary. Overall, the two-morphogen model can specify four boundaries (r2/r3, r3/r4, r4/r5 and r5/r6), while the one-morphogen model can specify only three boundaries (r2/r3, r3/r4 and r4/r5).

Additionally, we compared robustness in the two models with respect to initial hoxb1a expression. With constant initial hoxb1a level everywhere in space, we compared phase diagrams and resulting rhombomere lengths between the two-morphogen and one-morphogen models (Fig 3B, 3C, 3E and 3F). Interestingly, the inclusion of FGF makes the model relatively less sensitive to initial *hoxb1a* levels, in terms of the locations of gene expression boundaries and sizes of r3-5. When the initial hoxb1a level exceeds a certain level (e.g. 0.3), three rhombomeres (r3, r4 and r5) expand slightly along the A-P axis with r2/r3 and r3/r4 expanding anteriorly, and r4/r5 and r5/r6 expanding posteriorly (Fig 3B and 3C). In contrast, with RA alone, lengths of r3 and r4 are more sensitive to initial hoxb1a levels. In simulations with low initial hoxb1a levels (<0.2), r4 does not form (Fig 3E and 3F). As initial hoxb1a levels increase from 0.2 to 0.4, the r4 region rapidly expands at the expense of r3. A 15% increase in initial *hoxb1a* level (0.2–0.23) leads to an over two-fold expansion of r4 (21–44 μm) and r3 essentially vanishes when the initial *hoxb1a* level is close to 0.4. Thus, the two-morphogen model outperforms the one-morphogen model in robustness of rhombomere length, in that the second morphogen buffers responses to initial gene expression variation.



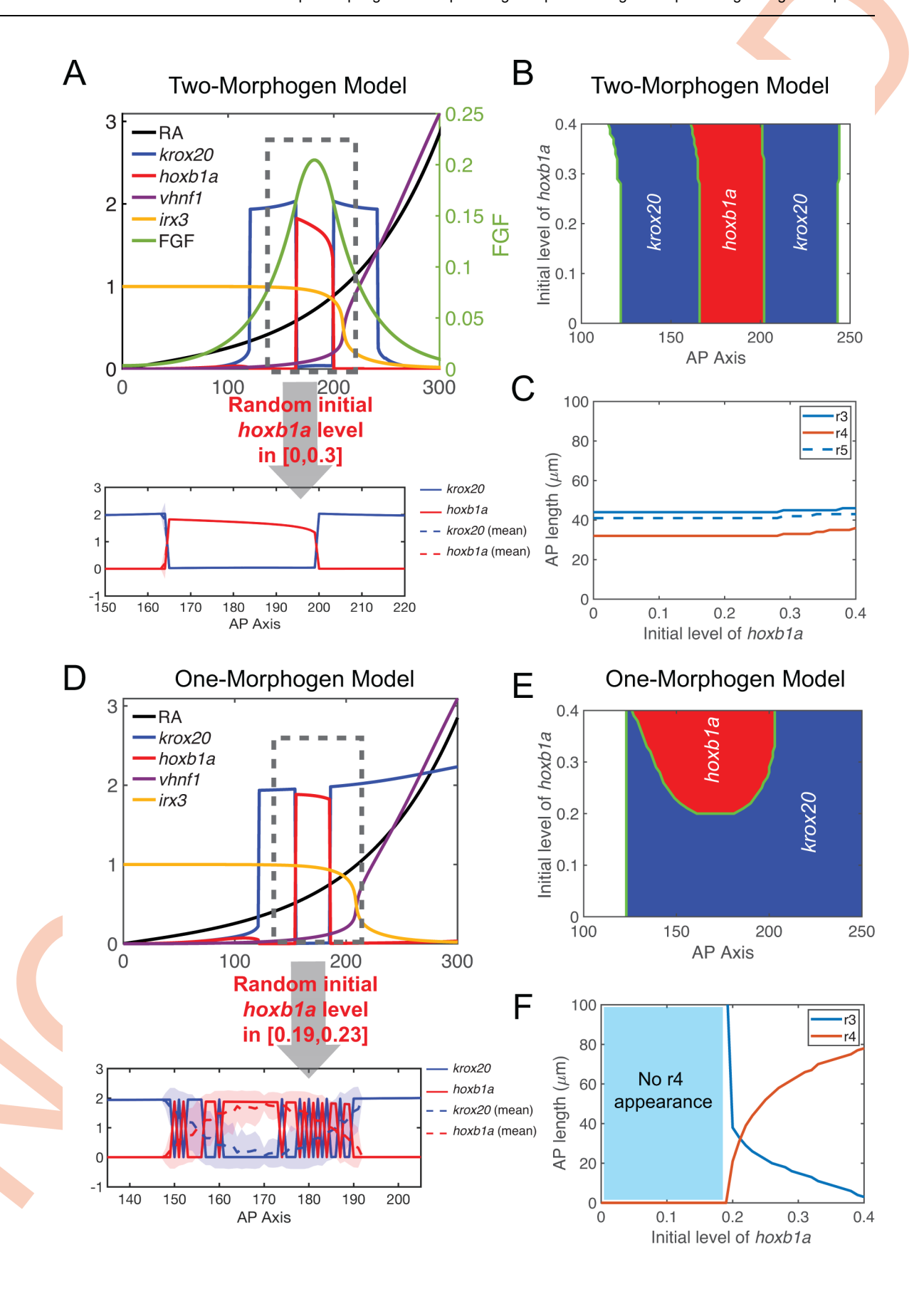


Fig 3. Comparing two-morphogen (RA, FGF) and one-morphogen (RA) models. (A-C) One-dimensional simulations for the two-morphogen model. (A) The upper panel shows spatial distributions of RA, krox20, hoxb1a, vhnf1, irx3 and FGF. The initial hoxb1a level is modeled as a constant 0.21 over the space. In the lower panel, the initial hoxb1a level is randomly sampled over the space independent of the location. The value is randomly uniformly distributed at a level of [0,0.3]. Solid line represents one simulation. Dashed line represents average values and the width of the shading around each line represents the standard deviation (n = 100). Since fluctuations over multiple simulations are small, solid lines overlap with dashed lines and the small standard deviations result in shadings of negligible width around the dashed lines. X-axis, microns; Y-axis, arbitrary units. (B) Phase diagram of hoxb1a and krox20 distributions with different initial hoxb1a levels. (C) Rhombomere lengths with different initial hoxb1a levels. (D-F) Similar one-dimensional simulations for the one-morphogen model. For (D), in the upper panel, the constant initial hoxb1a level is taken as 0.21; in the lower panel, the initial hoxb1a level is randomly sampled with levels in the range [0.19,0.23] with uniform distribution. Corresponding (E) phase diagram and (F) graph of rhombomere lengths with the one-morphogen model.

We also examined how the pattern reacts to perturbations of initial gene expression. We consider noisy initial *hoxb1a* levels over the space. In the two-morphogen model, such noise has negligible effects on later *hoxb1a* and *krox20* distributions resulting in clear segmental patterns and sharp r3/r4 and r4/r5 boundaries, and multiple simulations result in almost identical patterns (**Fig 3A**). However, in the one-morphogen model, *hoxb1a* and *krox20* distributions fluctuate more dramatically than the two-morphogen model. Despite a much smaller magnitude of perturbation (13%) in initial *hoxb1a* levels, the one-morphogen model shows fluctuating boundaries for both r3/r4 and r4/r5 (**Fig 3D**). Overall, the two-morphogen cooperation facilitates both accurate rhombomere lengths and sharp boundaries with perturbations of initial gene expression, providing robustness in patterning during the initial stages.

Rapid initial convergence improves boundary sharpness and segment size

Due to stochasticity, the initial pattern shows rough boundaries between rhombomeres. Later on, patterns sharpen and refine boundaries from 11–14 hpf. During these stages, the zebrafish hindbrain changes shape dramatically as it narrows in width along the L-R axis, extends in length along the A-P axis (Fig 1A) and thickens in the D-V axis [58]. We mainly studied A-P and L-R axes and their dimensions were experimentally measured (Fig 2A and 2B). Length along the A-P axis changes slowly during this period, but width along the L-R axis rapidly shrinks from 283 µm to 162 µm during the first hour, and further to 104 µm during the last two hours with approximately a 75% drop in the average rate after which patterning is largely complete. To determine how such rapid initial convergence influences hindbrain patterning we compared models incorporating medium or slow initial convergence with the rapid initial convergence rate we measured experimentally. All three types of convergence have the same initial and terminal L-R width. The curve of the medium convergence is taken as a linear function. The curves of the slow and rapid initial convergences are symmetric to the linear curve (Fig 4A).

We first performed simulations with full models including both gene regulation and cell sorting. Regardless of the convergence speed, most cells segregate to their correct territories and the final patterns display sharp boundaries between rhombomeres (Fig 4B-4E). Rapid initial convergence allows the sharpest boundaries and the fewest DCs while slow initial convergence results in the roughest boundaries and more DCs (Fig 4F). SI and DC numbers at 14 hpf in multiple independent simulations confirm conclusions based on single simulations (Fig 4H and 4I). The exception is that rapid and medium convergence rates yield similar SI at the r5/r6 boundary and DC numbers (Fig 4H and 4I). Rhombomere A-P lengths also vary greatly in this model with different convergence rates (Fig 4G). Simulations with slow initial convergence result in all three rhombomeres (r3-5) elongated. Simulations with medium convergence result in a shorter r5 compared to r3 and r4. Simulations with rapid initial convergence result in r3-5 being all roughly the same length (with r4 slightly shorter) similar to experimental measurements of the hindbrain at 14 hpf (Figs 2H and 4G).



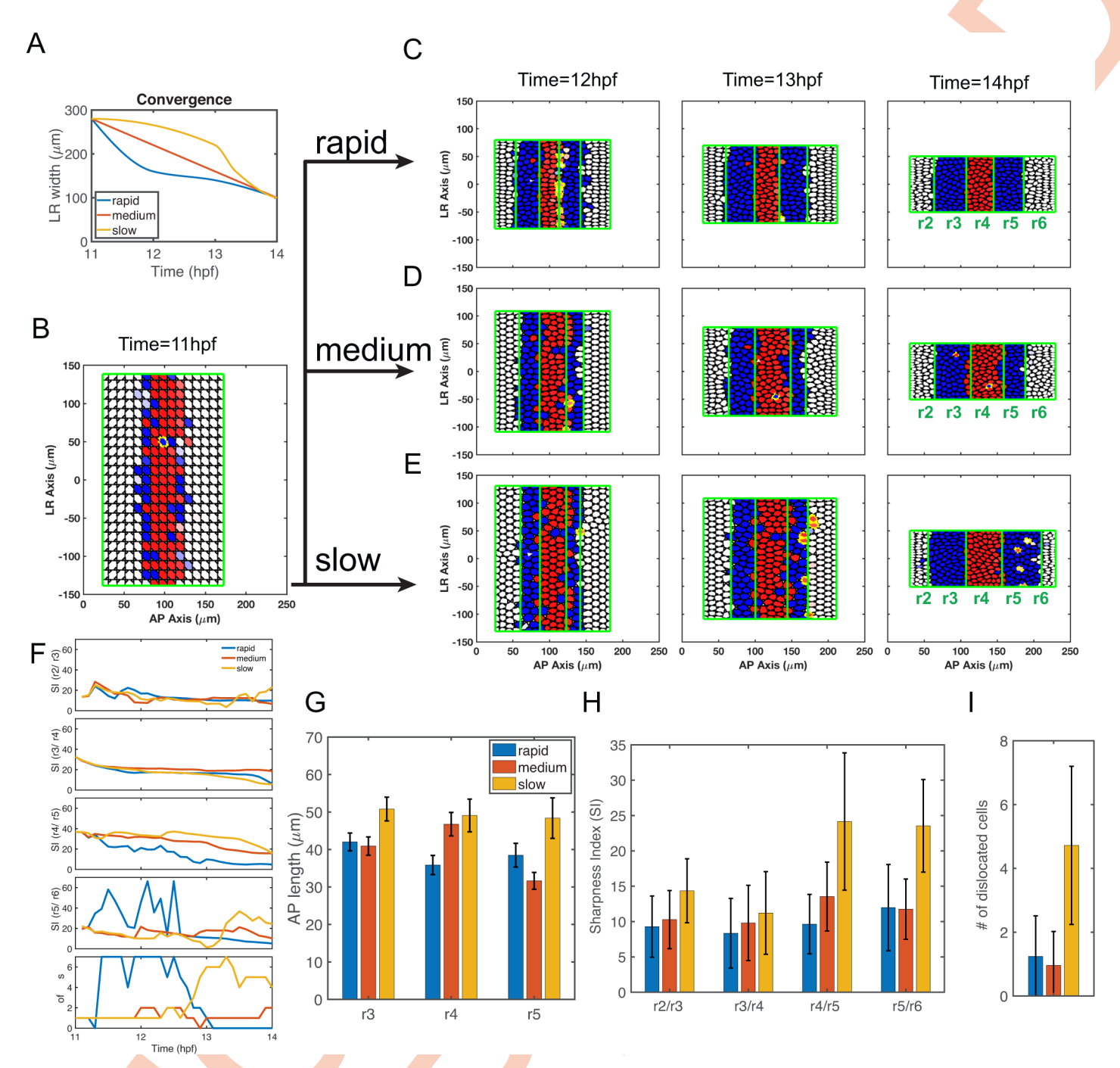


Fig 4. Simulations of full models combining gene regulation and cell sorting with different convergence rates. (A) Three convergence rates during the 11–14 hpf period are considered in the model, rapid (from experimental measurements, Fig 2B), medium and slow. All start and terminate with the same L-R width. The curve of medium convergence is depicted as a linear function. The curve of slow initial convergence is symmetric to the curve of rapid initial convergence with respect to the curve of linear function. (B-E) Time series of cell distributions with different convergence rates from 11–14 hpf. hoxb1a (red) and krox20 (blue) expression. Dislocated cells (DCs) are highlighted by yellow edges. (B) Three simulations start with the same initial cell distribution (11 hpf) generated by the gene expression model (see Methods). Cell distributions with (C) rapid, (D) medium and (E) slow initial convergence rates from 12–14 hpf. (F) The boundary sharpness index (SI) for four boundaries (SI(r2/r3), SI(r3/r4), SI(r4/r5) and SI(r5/r6)) and DC number versus time. (G-I) Histograms depicting three convergence rates analyzed for (G) rhombomere lengths of r3-5, (H) SI and (I) DC number. Each represents 100 independent stochastic simulations for each convergence rate based on the same parameters. Error bars represent standard deviation.

Taken together, rapid initial convergence facilitates robust patterns by optimizing boundary sharpness and rhombomere A-P length. These influences depend on multiple mechanisms, including cell sorting and gene regulation, and their coordination.

Rapid initial convergence improves boundary sharpness through cell sorting. Next, we performed simulations with models incorporating cell sorting alone and excluding gene regulation using the cell sorting-only model. Initial "salt-and-pepper" cell distributions by assigning each cell an identity generated the five-segment pattern with rough boundaries (Fig 5A). Similar to observations in full models (Fig 4), most cells segregate to their correct territories and the final patterns display sharp boundaries between rhombomeres (Fig 5B–5D). Rapid initial convergence allows the sharpest boundaries and the fewest DCs, while slow initial convergence results in the roughest boundaries and more DCs (Fig 5E). SI and DC numbers at 14 hpf in multiple independent simulations confirm conclusions based on single simulations (Fig 5G and 5H). In the model with cell sorting alone, while these different speeds of convergence have major effects on boundary sharpness, they have relatively minor effects on rhombomere A-P length (Fig 5F). These results suggest rapid initial convergence improves boundary sharpness by facilitating the efficiency of cell sorting.

Rapid initial convergence helps specify correct rhombomere lengths by regulating cell fate. To investigate the effects of convergence on rhombomere lengths, we studied dynamics of gene expression under different convergence rates. We first investigated the influence of convergence rate on spatiotemporal dynamics of morphogen distribution and cell fate commitment (Fig 6). With rapid initial convergence, the RA signal and its direct target, vhnf1, increase quickly from 11–12 hpf, particularly in the posterior hindbrain (150 μm and 200 μm in Fig 6A and 6B), then decrease gradually. Near the r4/r5 boundary, hoxb1a is repressed by the increasing levels of vhnf1. FGF made in r4 then activates krox20 leading to identity switching for cells near the r4/r5 boundary with low hoxb1a expression (Fig 4C). With medium or slow initial convergence, the RA signal and vhnf1 remain relatively unchanged compared to rapid initial convergence (Fig 6A and 6B). Indeed, we observed that fewer cells switch from an r4 to an r5 identity and the r4/r5 boundary is located further posteriorly with medium or slow initial convergence (Fig 4C-4E). Similar to RA, FGF levels increase and peak around 12 hpf with models that include rapid initial convergence (Fig 6C). With medium convergence, FGF levels remain relatively unchanged, while with slow initial convergence, FGF levels remain unchanged at the early stage then increase and peak quickly at 13–14 hpf. At the same A-P position, slow initial convergence results in higher maximum FGF levels than rapid or medium convergence rates, Since FGF induces krox20 expression to drive identity switching from r2 identity to r3 (and r6 to r5) identity, the higher maximum FGF levels that result from slow initial convergence lead to displacement of the r2/r3 boundary anteriorly and the r5/6 boundary further posteriorly than rapid or medium convergence rates.

The different rhombomere A-P lengths under different convergence rates can be observed consistently either in the full model (Fig 4) or in the model excluding cell sorting (S2 Fig). The dynamics of the morphogens provides an explanation for the length behaviors. Rapid initial convergence leads to the smallest r4 because more r4 cells switch to r5 identities near the r4/r5 boundary. Slow initial convergence leads to a larger r3 and r5 because more r2 or r6 cells switch to r3 or r5 identities. Medium convergence results in the smallest r5 because fewer cells switch near the r4/r5 boundary than rapid initial convergence and fewer cells switch near the r5/r6 boundary than with slow initial convergence.

Interestingly, r3 emerges earlier and it initially has a larger A-P length than r5 since *vhnf1* expressed posteriorly represses the FGF activator, *hoxb1a*, resulting in weaker FGF signaling in r5 (**Fig 4B**). Through rapid convergence, r4 cells can switch to an r5 identity to compensate for the difference between r3 and r5 lengths to achieve correct A-P rhombomere lengths similar to experimental measurements.



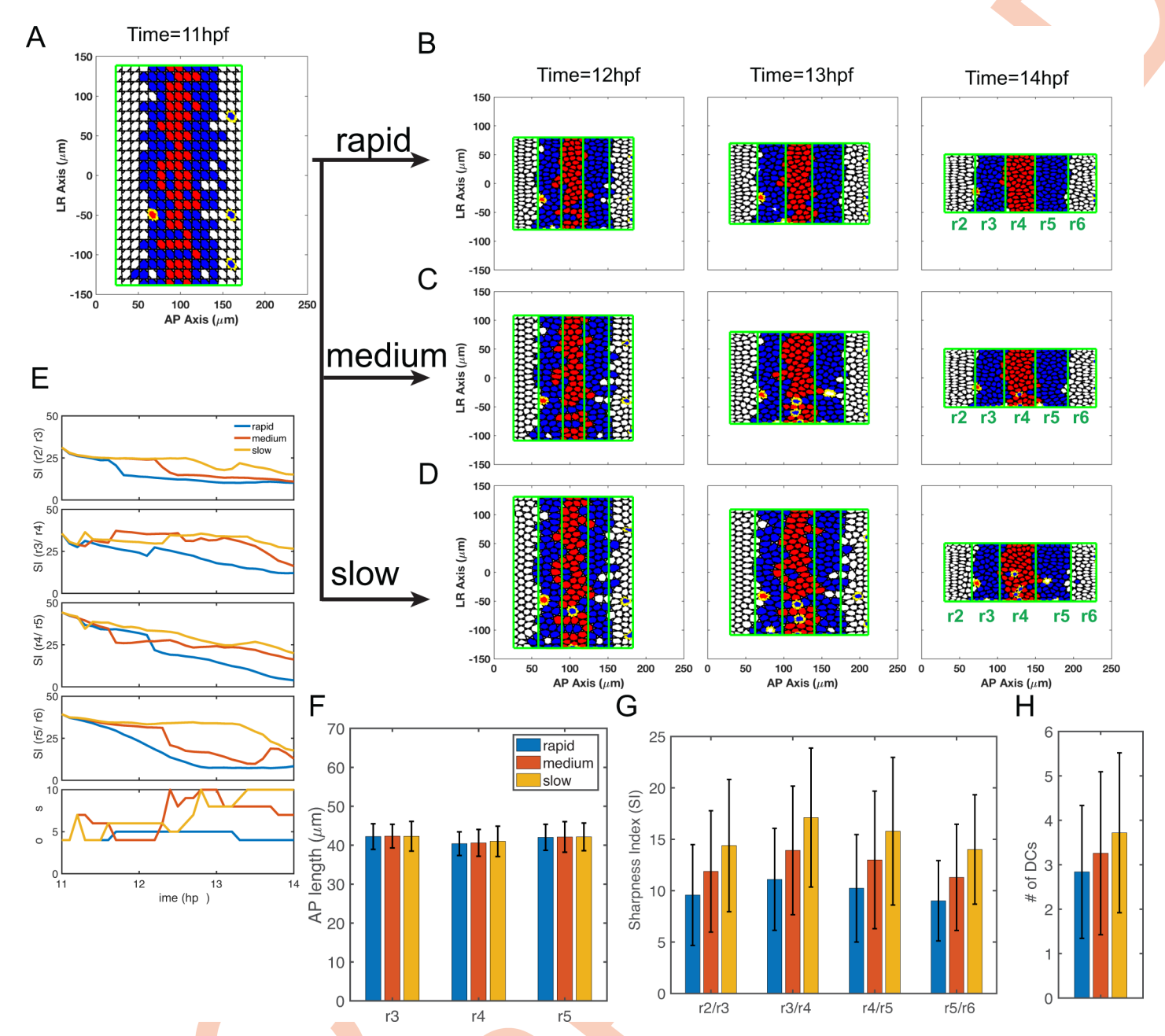


Fig 5. Simulations with selective cell-cell adhesion/sorting alone with different convergence rates. (A-D) Time series of cell distributions with different convergence rates from 11 to 14 hpf. hoxb1a (red) and krox20 (blue) expression. Dislocated cells (DCs) are highlighted by yellow edges. (A) Three simulations start with the same initial cell distribution (11 hpf) generated by the Gaussian mixture distribution. Cell distributions with (B) rapid, (C) medium and (D) slow initial convergence from 12–14 hpf. (E) The boundary sharpness index (SI) for four boundaries (SI(r2/r3), SI(r3/r4), SI(r4/r5) and SI(r5/r6)) and number of DCs versus time. (F-H) Histograms depicted three convergence rates analyzed for their (F) rhombomere lengths of r3-5, (G) SI and (H) the DC number. Each represents 100 independent stochastic simulations for each convergence rate are based on the same parameters. Error bars represent standard deviation.

Rapid initial convergence improves boundary sharpness through synergy between gene regulation and cell sorting

To study potential coordination between gene regulation and cell sorting in boundary formation, we restricted them individually at different patterning stages. Cells switch their fates at early stages of boundary sharpening (11–12 hpf) and this early gene regulation is critical for

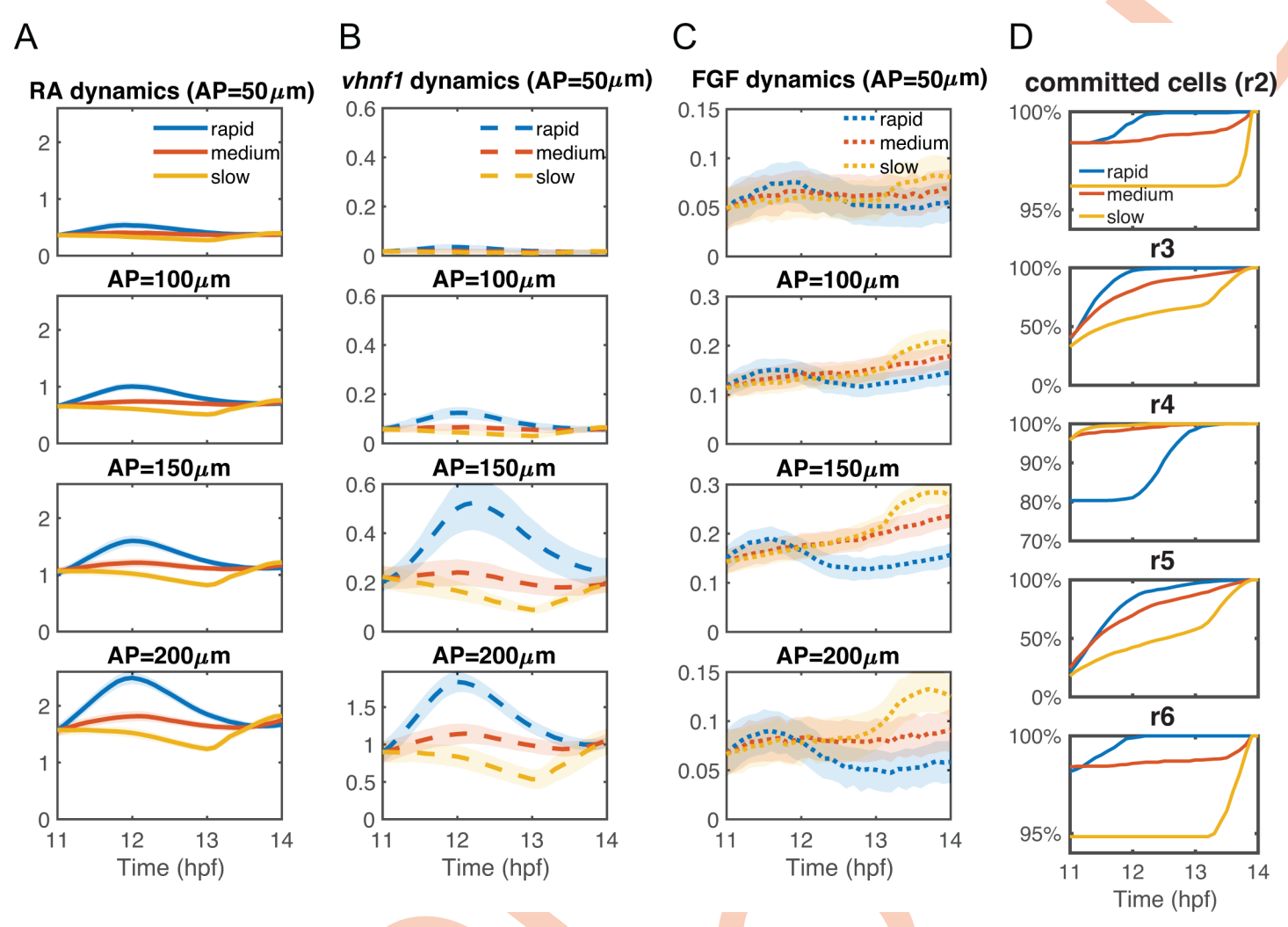


Fig 6. Dynamics of morphogens and cell commitment time with different convergence rates. The statistics of the dynamics of (A) intracellular RA [RA]_{im} (B) vhnf1, and (C) FGF signaling [FGF]_{signal} at different A-P lengths of the tissue domain: 50 μm, 100 μm, 150 μm and 200 μm. Lines represent average values and the width of the shading around each line represents the standard deviation. (D) The temporal dynamics of total percentages of cells that have committed in each rhombomere (r2-r6). Each panel shows the dynamics of the percentages of cells that have committed in each rhombomere. Data are collected from the full models, see Fig 4.

pattern establishment (Fig 2E). Therefore, to investigate if gene regulation also impacts pattern refinement later we extend the gene regulation period one additional hour at a time while maintaining cell sorting throughout the simulations (S3 Fig). Boundary sharpness improved with longer periods of gene regulation, depending on the stage. Extension by one hour, from 11–12 hpf to 11–13 hpf, significantly changed segment size, improved boundary sharpness, and reduced the number of DCs (S3B, S3C and S3F–S3H Fig). Extension by an additional hour from 11–13 hpf to 11–14 hpf had negligible effects on segment size, and minor improvements in boundary sharpness and DC numbers (S3C, S3D and S3F–S3H Fig). Conversely, with gene regulation throughout the simulations, limiting selective cell sorting to one-hour intervals within 11–14 hpf (with cells allowed to sort uniformly at other times) yields the worst patterns when limited to 11–12 hpf (S4 Fig). These results suggest that gene regulation is more important during early patterning stages and cell sorting later for boundary sharpening.

As shown in the previous subsection, with rapid initial convergence rates morphogen levels increase and peak at around 12 hpf, while morphogen levels increase and peak much later with

medium or slow initial convergence. Since *hoxb1a* and *krox20* are direct targets of RA and FGF, respectively, the timing of cell commitment as measured by expression of these genes is closely tied to the timing of peak morphogen levels. Consequently, rapid initial convergence drives the earliest cell commitment at around 12 hpf. Slow initial convergence leads to much later cell commitment (Fig 6D). One notable exception is that r4 cells commit later in the case of rapid initial convergence, due to switching near the r4/r5 boundary, but most cells still commit before 13 hpf (Fig 6D). Driven by early cell commitment, rapid initial convergence extends the effective period of cell sorting and shortens the effective period of gene regulation to improve boundary sharpness.

Rapid initial convergence mediates the trade-off between rhombomere length and boundary sharpness. To examine the sensitivity of our observations to model parameters, we performed a large number of simulations with random parameters, assaying both rhombomere A-P length and boundary sharpness. Using n=1000 independent repeats for each convergence rate, we found 513, 563 and 452 simulations that successfully produced a five-segment pattern for rapid, medium and slow initial convergence, respectively.

These results also revealed a trade-off between rhombomere length and sharpness, i.e. reduced length typically resulted in higher Sis, indicating rougher boundaries (**Figs 7** and **S5**). This can likely be explained by the fact that a shorter rhombomere has fewer cells with the same identity, thus cell sorting has less effect and cells are more susceptible to noise. As a result, a single stray cell has more impact on the boundary sharpness index. Such trade-offs are also observed for the model without convergent extension, leading to shorter and rougher rhombomere lengths (**Section 11 in S1 Text**). With shorter rhombomeres, rapid initial convergence significantly reduces this trade-off, particularly in r4 and r5 (**Figs 7** and **S5**).

Moreover, we quantified fractions of simulations achieving roughly equal segment length. We considered a simulation having equal rhombomere lengths if A-P lengths of r3, r4 and r5 were close to their experimentally measured average lengths within ranges $[m^*(100\%-d\%), m^*(100\%+d\%)]$, where m was the measured average length (Table G in S1 Text). With any values of deviation d, there are higher fractions of simulations achieving roughly equal length under rapid initial convergence compared to medium and slow initial convergence at 14 hpf (Fig 7G). Experimentally, standard deviations of r3, r4 and r5 length are within the range between 10% and 15% (Table G in S1 Text). Within this range of d, rapid initial convergence has at least 69% and 175% higher fractions of simulations achieving roughly equal segment length than medium and slow initial convergence, respectively (Fig 7G). These results are consistent with our findings that rapid initial convergence generates more accurate lengths of rhombomere and sharper boundaries.

Discussion

Our models suggest that a combination of two morphogens and rapid initial tissue convergence together drive robust hindbrain segmentation. Inclusion in the model of the short-range morphogen (FGF) secreted from r4, combined with the longer-range morphogen (RA) secreted posteriorly, substantially improves the robustness of segmental patterning compared with RA alone. Cooperation between morphogens is common in pattern formation in many contexts, in part because it helps maintain accuracy in size and boundary sharpness of target gene expression domains. Our previous models and experiments in the hindbrain have focused primarily on the r4/r5 boundary, where many gene regulatory interactions are known and the RA gradient is relatively steep [17,49,50]. The current model expands upon this work to explain the formation of other rhombomere boundaries, particularly r2/r3, r3/r4 and r5/r6, with the additional positional information provided by FGF. Surprisingly, rapid initial convergence dramatically improves robustness of rhombomere patterning, both segment size and



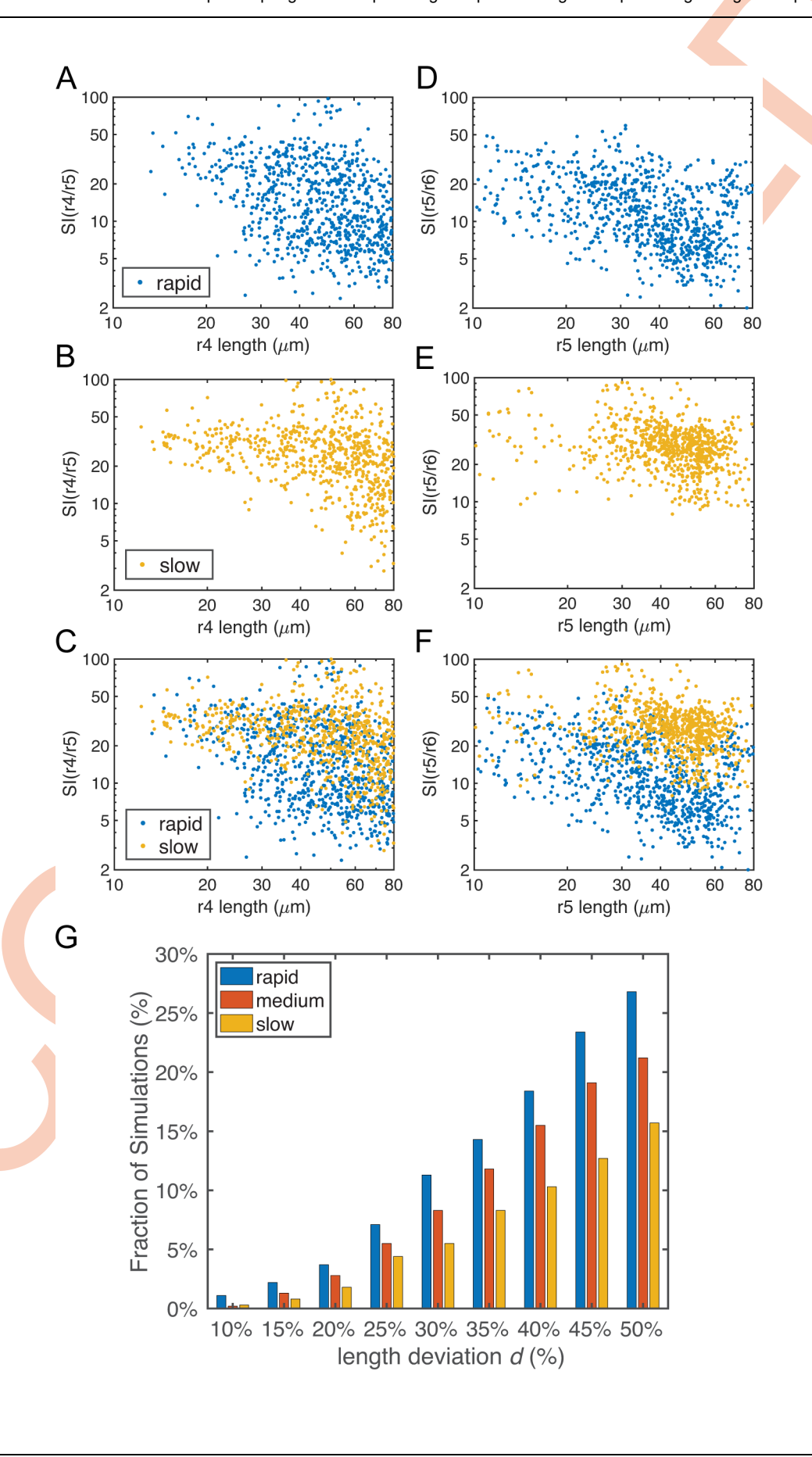


Fig 7. Boundary sharpness and rhombomere lengths based on simulations with random parameters in gene regulation. Parameters for gene regulation were randomly perturbed and a total of n=1000 simulations are displayed for each convergence rate. There are 513, 563 and 452 simulations for rapid, medium and slow initial convergence, respectively, which successfully generate the r2-6 pattern with four boundaries. (A-F) Dot plots showing the relationship between rhombomere length and boundary sharpness. Each point represents the corresponding quantities for each simulation. (A-C) Length of r4 versus sharpness index (SI) of the r4/r5 boundary with: (A) rapid initial convergence, (B) slow initial convergence and (C) a comparison between rapid and slow initial convergence. (D-F) Length of r5 versus SI of r5/r6 boundary with: (D) rapid initial convergence, (E) slow initial convergence and (F) a comparison between rapid and slow initial convergence. (G) Fractions of simulations achieving roughly equal rhombomere lengths versus the deviation d%. With a deviation d, a simulation has roughly equal rhombomere lengths if the length of each rhombomere is deviated at most d% from its average experimental length (i.e. r3, r4 and r5 are in the ranges of $42^*(100\%\pm d\%)~\mu m$, $34^*(100\%\pm d\%)~\mu m$ and $37^*(100\%\pm d\%)~\mu m$, respectively).

boundary sharpness. Rapid initial convergence may also be a conserved strategy for precise establishment of gene expression domains in other embryonic tissues that elongate by convergent extension [59–61] such as axial mesoderm in early vertebrate embryos [62] or stacking of chondrocytes in developing cartilages [63,64].

Complementary roles of long- and short-range morphogens in pattern accuracy and precision

In morphogen gradient-mediated patterning, it is crucial not only that target gene expression boundaries are accurately positioned but also that they are sharp. However, there is a trade-off between accuracy and precision of boundary patterning that depends on morphogen gradient steepness [1,27]. A steep morphogen gradient specifies boundary locations more precisely in the face of fluctuations in signal, is less sensitive to noise and facilitates boundary sharpness. However, the trade-off is that it makes positioning boundaries more sensitive to perturbations or noise in morphogen synthesis, slight shifts in which can move the boundaries along the A-P axis. Since RA is responsible for the initial A-P patterning of the hindbrain, starting from gastrulation, it likely plays a more prominent role in accuracy, due to its shallow distribution across much of the patterning region [40] and self-enhanced degradation [28]. On the other hand, FGF likely plays a prominent role in precision to help improve the sharpness of boundaries adjacent to its source, since its gradients are likely steeper due to its local effects [41,45,55]. In addition, FGF synthesis most likely varies less since one of its upstream regulators, hoxb1a, is bi-stable and tightly controlled by a complex network [46,47,65]. Together, these complementary features of the long-range shallow RA gradient and the short-range steep FGF gradient help overcome the trade-offs inherent in morphogen patterning systems for achieving both accurate and precise rhombomere pattern.

During hindbrain segmentation, r4 becomes the secondary signaling center that produces FGFs (e.g. Fgf4 and Fgf8) in zebrafish [41,42,45,55] that are regulated by the posteriorizing signal RA [28]. The MHB is another secondary FGF (i.e. Fgf8 in zebrafish) signaling center that likely contributes to anterior rhombomere patterning [66]. In many biological contexts, two morphogens interact with each other to facilitate spatial pattern formation. Interactions between the long- and short-range morphogens induce Turing patterns, such as Sox9 and Bmp in digit patterning [12], Edar and FGF in murine tooth development [67], FGF and Shh in limb regeneration [68], and Nodal and Lefty in early mesoderm formation and left-right patterning [69,70]. Two long-range morphogens with anti-parallel distributions improve the precision of a single boundary, such as Bcd and Cad in *Drosophila* embryo segmentation [71], and Bmp and Shh in vertebrate neural tube patterning [14,71,72]. Unlike these examples, the novel two-morphogen mechanism presented in this work includes one long-range and one short-range morphogen that act in parallel on downstream targets. This system specifies multiple boundaries of gene expression and improves both accuracy and precision of segmental patterns.



Rapid initial convergence in tissue morphogenesis improves pattern robustness

Intuitively, elongation along the A-P axis might be expected to hinder segmental patterning and rhombomere boundary sharpening [17], since cells quickly change neighbors and intercalate. However, we find quite the opposite (Fig 8). Rapid initial convergence facilitates boundary sharpening through two strategies. First, it induces efficientcell-cell contacts, consequently more efficient cell sorting, leading to sharper boundaries (Fig 8B). Second, it induces an early peak of morphogens that can result in early cell commitment, allowing cell sorting sufficient time for rearrangements without disrupting cell fate switching (Fig 8C). Rapid initial convergence can also regulate rhombomere length through morphogen dynamics. Initially the length of r5 is shorter than r3. Through a steeper RA distribution induced by rapid initial convergence, cells switch from an r4 to an r5 leading to similar r3 and r5 lengths (Fig 8A).

Another consequence of convergent extension is the movement of morphogen production and responding cells relative to one another. RA levels increase with time during early stages of hindbrain development due to increased synthesis and accumulation [39], then decrease due to the movement of the source of RA (aldha1a expression) further posteriorly as the body axis elongates [39,46,47]. Our model successfully recapitulates these RA dynamics (Fig 6A), which are also critical for specifying rhombomeres of the correct length and boundary sharpness. Previous manipulations of convergent extension in early zebrafish or mouse embryos, which result in a shortened body axis, have shown that convergent extension is critical in establishing signaling gradients and subsequently maintaining robust segmental patterning of the hindbrain, consistent with our results [73,74].

As tissue deforms, extracellular morphogens may have both active motion driven by the tissue dynamics as well as movements of the signals induced by morphogens within cells. In our model, both extra and intracellular morphogens were modeled in continuum context with Eulerian coordinates, where the advections are usually required to capture morphogen dynamics with moving boundaries [75]. We found that even if we removed intracellular advections from the models, our main results showing a positive influence of rapid initial convergence on patterning remain (S11 Fig).

Tissue size, thickening and additional signals in hindbrain patterning

The embryonic zebrafish hindbrain is extremely small and composed of relatively few cells compared with most other vertebrates [49,76,77]. The actual A-P length of each rhombomere at the stages we have examined (11–14 hpf) is approximately 3~5 cell-diameters. This small size presents a challenge for sharpening rhombomere boundaries, where a few neighbor cells with the same identity provide weak adhesion during sorting, and even more so for generating a series of rhombomeres of similar size. A rapid initial convergence rate may be particularly important for coordinating size and boundary sharpness in such a miniaturized embryo. However, given the conserved patterns of gene expression and neuronal differentiation observed in hindbrains across species, we are confident that many of the same rules apply.

Our modeling and experimental measurements correspond in many respects, including the dynamics of RA synthesis and FGF4/8 expression as well as *hoxb1a*, *krox20*, *vhnf1* and *irx3* expression in zebrafish. However, many questions remain. In our simulations, DCs remain in r2 and r6 due to randomness in gene expression. For example, in some cases *hoxb1a*+ cells are observed in r2 because of early increases in RA, which induce *hoxb1a*. The model cannot account for how these cells switch to their correct segmental identities, but perhaps they are displaced along the D-V axis, undergo apoptosis or are extruded from the hindbrain. Such switching may also reflect a "community effect" by which cells switch identity depending on the

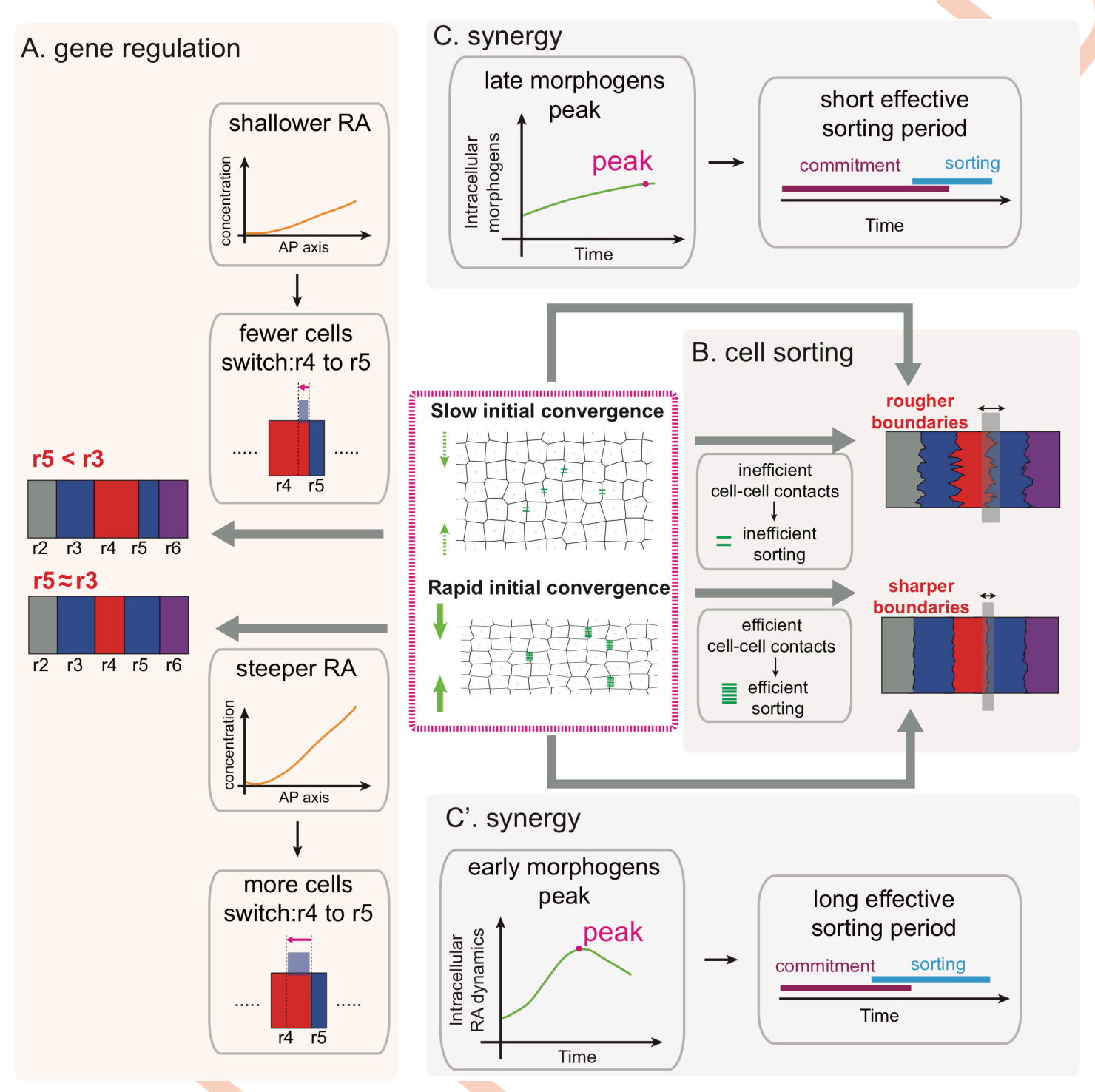


Fig 8. Schematic illustration for rapid initial convergence improves pattern robustness by comparing with slow initial convergence (A) Gene regulation/cell fate: rapid initial convergence produces a steeper RA distribution to induce more cells switching from r4 (red) to r5 (blue) identity than slow initial convergence. Consequently, r5 has similar size with r3, consistent with the experimental measurements. (B) Cell sorting: rapid initial convergence increases cell-cell contacts to enhance efficiency of cell sorting, leading to sharper boundaries comparing to slow initial convergence. Number of green lines represent efficiency of cell sorting. (C-C') Synergy between cell sorting and gene regulation: rapid initial convergence induces an early peak of morphogens for both RA and FGF, leading to an early commitment of cell fates. Cell sorting mechanisms fully function to sharpen boundaries with sufficient time without disrupting cell fate switching.

collective influences of their neighbors, but the underlying mechanisms have not been fully identified [34,49]. Gene regulatory networks with other signals involved may also prevent cell switching or sorting by regulating *hoxb1a* or *krox20*. For example, Fgf8 is expressed at the MHB in zebrafish embryos starting at 10 hpf, and likely important for the patterning of more anterior rhombomeres, r1-3, which will be interesting to consider in future models [47,66]. Wnt is another morphogen that controls early anterior rhombomeres and MHB formation [47,78].

Many other features of tissue morphogenesis also need to be considered for a comprehensive three-dimensional model of hindbrain segmentation. During the patterning period considered here, cells divide and the NP thickens along the D-V axis [58]. While cells divide in this period, the NP thickens and cell number in the two-dimensional plane (A-P and L-R plane) changes very little [58]. We also studied a two-dimensional model that incorporates cell proliferation and growth and while this led to tighter cell distributions and higher variations in rhombomere length than in other models, overall it confirmed that rapid initial convergence improves pattern robustness (Section 10 in S1 Text). The two-dimensional nature of our models, which do not consider the complicated dynamics associated with proliferation and thickening along the D-V axis, likely explains why the computed rhombomere lengths in our model do not perfectly fit the experimental measurements (Fig 2H). More realistic, three-dimensional models that incorporate these components pose an exciting challenge and opportunity for the future.

Methods

Ethics statement

All animal work performed in this study was approved by the University of California Irvine Institutional Animal Care and Use Committee (Protocol #AUP-20-145).

Animal husbandry

All animals used in this study were raised and handled in accordance with the guidelines of the Institutional Animal Care and Use Committee at University of California, Irvine. AB strain embryos were collected from natural crosses, raised at 28.5°C in embryo medium (EM), and staged as previously described [79].

Whole-mount in situ hybridization

In situ hybridization was performed on whole embryos as previously described [80]. Digoxygenin- and fluorescein-labelled riboprobes for *aldh1a2* [81], *krox20* [82], *otx2* [83] were synthesized using an RNA labelling kit (Roche) from cDNA that had been previously cloned into PCS2+ plasmids and linearized.

Imaging and measurement of hindbrain

Embryos were flat mounted in glycerol as previously described [84] and imaged on a Zeiss Axioplan 2 compound microscope equipped with a Micropublisher 5.0 RTV camera with Zeiss ZEN 3.1 (blue edition) software. Hindbrain measurements were performed using ImageJ/Fiji software.

Computational domains of the model

The entire hindbrain along with the RA production region, modeled as the "morphogen domain", is used to model the diffusion and distribution of morphogens (Fig 1B). In the two-dimensional model, the morphogen domain is assumed as a rectangle with the anterior-posterior (A-P) axis as its length and the left-right (L-R) axis as its width. We take the posterior end

of the MHB, defined by otx2 expression, as the anterior limit of the domain, $x^{(1)} = 0$ and the posterior end of the RA production region, defined by aldh1a2 expression, as its posterior limit, $x^{(1)} = L_1(t)$. The L-R width of the hindbrain is $L_2(t)$. The morphogen domain has a rectangular structure with dynamic sizes:

$$M(t) = \left\{ \left(x^{(1)}, x^{(2)} \right) \in H : H = [0, L_1(t)] x \left[-\frac{1}{2} L_2(t), \frac{1}{2} L_2(t) \right] \right\} \tag{1}$$

The RA production region is modeled as:

$$P(t) = \left\{ \left(x^{(1)}, x^{(2)} \right) : \left(x^{(1)}, x^{(2)} \right) \in [p(t), L_1(t)] \\ x[-\frac{1}{2}L_2(t), \frac{1}{2}L_2(t)] \right\}, \tag{2}$$

where p(t) is the A-P position of the anterior boundary of the RA production region at time t. $L_1(t)$, $L_2(t)$ and p(t) are obtained from experimental measurements made in zebrafish embryos at 11, 12, 13 and 14 hours postfertilization (hpf). A cubic interpolation is used to obtain the smooth curves (Fig 2A and 2B).

Individual cells are modeled in a "tissue domain" that is contained within the morphogen domain. The tissue domain shares the same L-R axis with of the morphogen domain and its A-P range is proportional to the range of morphogen:

$$T(t) = \left\{ \left(x^{(1)}, x^{(2)} \right) : \left(x^{(1)}, x^{(2)} \right) \in [r_1 L_1(t), r_2 L_1(t)] \\ x[-\frac{1}{2} L_2(t), \frac{1}{2} L_2(t)] \right\} \tag{3}$$

where r_1 and r_2 are constants given in the **Table A in S1 Text**. At $x = (x_1, x_2)$, the growth velocity of the tissue is given by

$$V(\mathbf{x},t) = \left(L_1'(t)\frac{x^{(1)}}{L_1(t)}, L_2'(t)\frac{x^{(2)}}{L_2(t)}\right). \tag{4}$$

Stochastic dynamics of morphogens

To model morphogen dynamics in the growing hindbrain, we use stochastic convection-reaction-diffusion equations. The equations for RA are given by

$$\frac{\partial [RA]_{out}}{\partial t} + \nabla \cdot (V[RA]_{out}) = D_r \Delta [RA]_{out} + A(x, t) \xrightarrow{\text{noise}} + k_r [RA]_{in} - (1 + \beta_r) k_r [RA]_{out} f_1 + \mu_{r1} \frac{dw_{r1}(t)}{dt},$$

$$\frac{\partial [RA]_{in}}{\partial t} + \nabla \cdot (V[RA]_{in}) = k_r [RA]_{out} - k_r [RA]_{in} - d_r (x^{(1)}) [RA]_{in}$$

$$+ \mu_{r2} \frac{dw_{r2}(t)}{dt}, \qquad (5)$$

where $[RA]_{out}$ and $[RA]_{in}$ are extracellular and intracellular forms of RA, respectively. $\mu_{r1} \frac{dw_{r1}(t)}{dt}$ and $\mu_{r2} \frac{dw_{r2}(t)}{dt}$ are additive white noise. The convection term describes the dilution and advection of RA caused by convergence extension. The production is confined to the RA production region and modeled by a Hill function of AP position $x^{(1)}$ with a large Hill coefficient:

$$A(\mathbf{x},t) = \frac{\nu_r}{1 + \left(\frac{x_1}{p(t)}\right)^{-20}}.$$
(6)

In f_1 and f_2 , k_r is the rate of exchange of morphogen between intracellular and extracellular forms. The rate of extracellular morphogen degradation is taken as a constant $\beta_r k_r$ and the



degradation of intracellular morphogen rate d_r is a piecewise function with

$$d_r(x^{(1)}) = \begin{cases} k_{\text{max}}, & \text{if } x^{(1)} > p(t), \\ k_0, & \text{otherwise.} \end{cases}$$
 (7)

The degradation rate in the RA production region has a large value k_{max} since the RA degrading enzyme cyp26a1 is expressed in the RA production region [28]. We use an absorbed boundary condition of $x^{(1)} = 0$ since cyp26a1 is highly expressed in the forebrain and MHB, providing a sink for RA. No-flux boundary conditions are used for the other three boundaries.

Similarly, we model both free diffusible FGF ([Fgf]_{free}) and FGF ([Fgf]_{signal}) signaling as the following:

$$\frac{\partial [Fgf]_{free}}{\partial t} + \nabla \cdot \left(V[Fgf]_{free} \right) = D_f \Delta [Fgf]_{free} + A_f([H], \mathbf{x}) + k_{rf}[Fgf]_{signal}
- (d_{f1} + k_f)[Fgf]_{free} + \mu_{f1} \frac{dw_{f1}(t)}{dt},
\frac{\partial [Fgf]_{signal}}{\partial t} + \nabla \cdot \left(V[Fgf]_{signal} \right) = k_f [Fgf]_{free} - k_{rf}[Fgf]_{signal}
- d_{f2}[Fgf]_{signal} + \mu_{f2} \frac{dw_{f2}(t)}{dt}.$$
(8)

The free diffusible FGF binds with its receptor to form a complex with rate $k_f[Fgf]_{free}$. The complex between FGF and its receptor represents the FGF signal ($[Fgf]_{signal}$) for simplification. The term $k_{rf}[Fgf]_{signal}$ describes the dissociation rate of the complex. d_{f1} and d_{f2} are degradation rates of free diffusible FGF and FGF signaling, respectively. The production of FGF is upregulated by hoxb1a and the production rate is modelled by a Hill function for hoxb1a:

$$A_f([H], \mathbf{x}) = \nu_f \frac{[H](\mathbf{x})^2}{1 + a_{hf}[H](\mathbf{x})^2}.$$
 (9)

The hoxb1a level [H] is defined at the center of each cell. In Eq (9), the term [H](x), defined at arbitrary location x, is obtained by interpolating [H] values with locations in cell centers (Section 1 in \$1 Text). No-flux boundary conditions are used for FGF at all four boundaries.

Stochastic dynamics of downstream genes

We model the dynamics of gene expression with a system of stochastic differential equations based on the gene network (Fig 1C). For the i-th cell centered at c_i , the equations for the gene expression are given by

$$\frac{d[H]_{i}}{dt} = v_{h} \frac{a_{hh}[H]_{i}^{2} + a_{rh}[RA]_{in}^{2}}{1 + a_{hh}[H]_{i}^{2} + a_{rh}[RA]_{in}^{2} + b_{kh}[K]_{i}^{2} + b_{vh}[V]_{i}^{2}} - d_{h}[H]_{i} + \mu_{h} \frac{dw_{h}}{dt},$$

$$\frac{d[K]_{i}}{dt} = v_{k} \frac{a_{kk}[K]_{i}^{2} + a_{fk}[Fgf]_{signal}^{2}}{1 + a_{kk}[K]_{i}^{2} + a_{fk}[Fgf]_{signal}^{2} + b_{hk}[H]_{i}^{2}} - d_{k}[K]_{i} + \mu_{k} \frac{dw_{k}}{dt},$$

$$\frac{d[V]_{i}}{dt} = v_{v} \frac{a_{rv}[RA]_{in}^{2}}{1 + a_{rv}[RA]_{in}^{2} + b_{iv}[I]_{i}^{2}} - d_{v}[V]_{i} + \mu_{v} \frac{dw_{v}}{dt},$$

$$\frac{d[I]_{i}}{dt} = v_{i} \frac{1}{1 + b_{vi}[V]_{i}^{2}} - d_{i}[I]_{i} + \mu_{i} \frac{dw_{i}}{dt},$$
(10)

where [H], [K], [V] and [I] are gene expression of hoxb1a, krox20, vhnf1 and irx3, respectively. $[RA]_{in} = [RA]_{in}|_{\mathbf{x}=\mathbf{c}_i}$ and $[Fgf]_{signal} = [Fgf]_{signal}|_{\mathbf{x}=\mathbf{c}_i}$ refer to the RA and FGF signaling levels at the center of i-th cell \mathbf{c}_i to provide spatial signals for cells.

Models for individual cells and their interactions

Following our previous study [16], we use the subcellular element method (SCEM) to model individual cells [56]. A total of N_{cell} = 345 cells are modeled in each simulation, where 23 rows and 15 columns of cells align uniformly in the rectangular tissue region at the initial stage (11 hpf). Each cell consists of sub-cellular elements (nodes) and interacts according to a prescribed intercellular force potential. A cell consists of $2N_{node}$ (N_{node} = 6) nodes and those nodes form two hexagonal layers (S6A Fig). The radius of the outer layer is R_{out} and the radius of the inner layer is R_{in} . Initially cells are uniformly distributed in the tissue domain (Fig 4B). For a system with N_{cell} cells and $2N_{node}$ nodes per cell, the location of i-th node in n-th cell $x_{n,i}$ is determined by the equation

$$\frac{d}{dt}\mathbf{x}_{n,i} = \mathbf{v}_{n,i}^{ext} + \mathbf{v}_{n,i}^{inter} + \mathbf{v}_{n,i}^{inner}.$$
(11)

On the right hand side, the first term represents cell migration due to convergent-extension [85,86]. It is given by

$$\begin{cases} \mathbf{v}_{n,j}^{\text{ext}} = \mathbf{V}(\mathbf{c}_n, t), \\ \mathbf{c}_n = \frac{1}{2N_{node}} \sum_{i=1}^{2N_{node}} \mathbf{x}_{n,i}. \end{cases}$$
(12)

The second term represents the forces between cells while the third term represents forces between nodes within the same cell to maintain stable cell morphologies [56] (see Section 2 in S1 Text).

Definition of boundary location (m), sharpness index (SI) and number of dislocated cells (DC)

To study boundary locations and sharpness quantitatively, we define three quantities: boundary location (m), boundary sharpness index (SI) and number of dislocated cells (DCs). For example, the A-P position of the r3/r4 boundary is denoted by m(r3/r4) and its boundary SI is denoted by SI(r3/r4). A cell is called a DC if: a) its identity is different from the segment in which it is located; b) its distance to the boundary of its correct segment is over three cell-diameters.

In a region with A-P coordinates in the range of (a,b), we split the index set of all cells into two sets S_L and S_R based on cell identities, where cells in S_L or S_R have segmental identities located anterior or posterior to this region. We define the distance function from the i-th cell centered at c_i to an arbitrary straight line with A-P position k (the potential location of boundary):

$$\operatorname{dis}(\boldsymbol{c}_{i},k) = \begin{cases} \operatorname{ReLU}(\boldsymbol{c}_{i}^{(1)} + r - k), & \text{if } i \in S_{L}, \\ \operatorname{ReLU}(-\boldsymbol{c}_{i}^{(1)} + r + k), & \text{if } i \in S_{R}, \end{cases}$$

$$(13)$$

where r is the radius of the cell, and

$$ReLU(x) = \begin{cases} x, & \text{if } x > 0, \\ 0, & \text{if } x \le 0, \end{cases}$$

is the rectified linear unit function. For a cell in S_L or S_R with non-zero distance, this distance

function calculates the Euclidean distance between the anterior or posterior distal ends of this cell to the potential location of boundary *k*. This distance function is illustrated in S6B Fig.

We quantify the boundary location (*m*), SI and number of DCs in this region, called *K*, by solving an optimization problem:

$$m_{K} = \operatorname{argmin}_{k \in (a,b)} \left(\sum_{\operatorname{dis}(\boldsymbol{c}_{i},k) \leq 6r} (\operatorname{dis}(\boldsymbol{c}_{i},k))^{2} \right)^{\frac{1}{2}},$$

$$SI_{K} = \min_{k \in (a,b)} \left(\sum_{\operatorname{dis}(\boldsymbol{c}_{i},k) \leq 6r} (\operatorname{dis}(\boldsymbol{c}_{i},k))^{2} \right)^{\frac{1}{2}},$$

$$DC_{K} = \left\{ k : \operatorname{dis}(\boldsymbol{c}_{i}, m_{R}) > 6R_{0} \right\}.$$

$$(14)$$

Particularly if the distance from a cell to the boundary is within three cell-diameters, the cell contributes to the boundary location and boundary SI. Otherwise, it is regarded as a DC and it does not contribute to the calculation of either boundary location or sharpness.

Next, we split all cells in the responding tissue domain with index set S into three sets with distinct cell types at time t. There are hoxb1a cells (S_h) , krox20 cells (S_k) and non-expressing cells (S_n) based on their expression level of hoxb1a and krox20.

$$S_{h} = \{i \in S : [H]_{i}(t) \ge 1.2\},$$

$$S_{k} = \{i \in S : [K]_{i}(t) \ge 1.2\},$$

$$S_{n} = \{i \in S : i \notin S_{h} \cup S_{k}\}.$$
(15)

Now, we calculate those quantities for four boundaries in the tissue domain one-by-one by utilizing Eq (14) and Eq (15) as shown in the flow below (Algorithm 1):

Algorithm 1. Calculate m, SI and DC for cells in domain with AP range $[r_1L_1(t), r_2L_1(t)]$

Step	$C = \operatorname{mean}_{i \in S_h}(c_i^{(1)})$	Find a point
1		to split the tissue domain
Step	$K_1 = [r_1 L_1(t), C],$ $m(r3/r4) = m_{K_1},$	Quantify r3/
2	$S_L = \{i \in S : i \in S_k \cup S_n \text{ and } c_i^{(1)} \in K_1\}, SI(r3/r4) = SI_{K_1},$	r4 boundary: hoxh1a cells
	$S_p = \{i \in S : i \in S_h \text{ and } c_i^{(1)} \in K_1\}, DC(r3/r4) = DC_{K_1}.$	are on the
		right and
		other cells are on the left.
Step	$K_2 = [C, r_2 L_1(t)], \qquad m(r4/r5) = m_{K_2},$	Quantify r4/
3	$S_{L} = \{ i \in S : i \in S_{h} \text{ and } c_{i}^{(1)} \in K_{2} \}, SI(r4/r5) = SI_{K_{2}},$	r5 boundary
	$S_R = \{i \in S : i \in S_k \cup S_n \text{ and } c_i^{(1)} \in K_2\}, DC(r4/r5) = DC_{K_2}.$	
Step	$m(r2/r3) = m_{K_3},$ $K_3 = [r_1L_1(t), m(r3/r4)],$	Quantify r2/
4	$\begin{cases} K_3 = [r_1 L_1(t), m(r3/r4)], \\ S_L = \{i \in S : i \in S_n \text{ and } \mathbf{c}_i^{(1)} \in K_3\}, S_R = \{i \in S : i \in S_k \text{ and } \mathbf{c}_i^{(1)} \in K_3\}, SI(r2/r3) = SI_{K_3}, \\ DC(r2/r3) = DC(r2/r3$	r3 boundary
	$S_L = \{i \in S : i \in S_n \text{ and } c_i^* \in K_3\}$ $DC(r2/r3) = DC_{K_3}.$	
Step	$m(r5/r6) = m_{K_4},$ $K_4 = [m(r4/r5), r_2L_1(t)],$	Quantify r5/
5	$\begin{cases} K_4 = [m(r^4/r^5), r_2L_1(t)], \\ S_L = \{i \in S : i \in S_k \text{ and } \mathbf{c}_i^{(1)} \in K_4\}, SI(r^5/r^6) = SI_{K_4}, \\ S_L = \{i \in S : i \in S_k \text{ and } \mathbf{c}_i^{(1)} \in K_4\}, SI(r^5/r^6) = SI_{K_4}, \\ S_L = \{i \in S : i \in S_k \text{ and } \mathbf{c}_i^{(1)} \in K_4\}, SI(r^5/r^6) = SI_{K_4}, \\ S_L = \{i \in S : i \in S_k \text{ and } \mathbf{c}_i^{(1)} \in K_4\}, SI(r^5/r^6) = SI_{K_4}, \\ S_L = \{i \in S : i \in S_k \text{ and } \mathbf{c}_i^{(1)} \in K_4\}, SI(r^5/r^6) = SI_{K_4}, \\ S_L = \{i \in S : i \in S_k \text{ and } \mathbf{c}_i^{(1)} \in K_4\}, SI(r^5/r^6) = SI_{K_4}, \\ S_L = \{i \in S : i \in S_k \text{ and } \mathbf{c}_i^{(1)} \in K_4\}, SI(r^5/r^6) = SI_{K_4}, \\ S_L = \{i \in S : i \in S_k \text{ and } \mathbf{c}_i^{(1)} \in K_4\}, SI(r^5/r^6) = SI_{K_4}, \\ S_L = \{i \in S : i \in S_k \text{ and } \mathbf{c}_i^{(1)} \in K_4\}, SI(r^5/r^6) = SI_{K_4}, \\ S_L = \{i \in S : i \in S_k \text{ and } \mathbf{c}_i^{(1)} \in K_4\}, SI(r^5/r^6) = SI_{K_4}, \\ S_L = \{i \in S : i \in S_k \text{ and } \mathbf{c}_i^{(1)} \in K_4\}, \\ S_L = \{i \in S : i \in S_k \text{ and } \mathbf{c}_i^{(1)} \in K_4\}, \\ S_L = \{i \in S : i \in S_k \text{ and } \mathbf{c}_i^{(1)} \in K_4\}, \\ S_L = \{i \in S : i \in S_k \text{ and } \mathbf{c}_i^{(1)} \in K_4\}, \\ S_L = \{i \in S : i \in S_k \text{ and } \mathbf{c}_i^{(1)} \in K_4\}, \\ S_L = \{i \in S : i \in S_k \text{ and } \mathbf{c}_i^{(1)} \in K_4\}, \\ S_L = \{i \in S : i \in S_k \text{ and } \mathbf{c}_i^{(1)} \in K_4\}, \\ S_L = \{i \in S : i \in S_k \text{ and } \mathbf{c}_i^{(1)} \in K_4\}, \\ S_L = \{i \in S : i \in S_k \text{ and } \mathbf{c}_i^{(1)} \in K_4\}, \\ S_L = \{i \in S : i \in S_k \text{ and } \mathbf{c}_i^{(1)} \in K_4\}, \\ S_L = \{i \in S : i \in S_k \text{ and } \mathbf{c}_i^{(1)} \in K_4\}, \\ S_L = \{i \in S : i \in S_k \text{ and } \mathbf{c}_i^{(1)} \in K_4\}, \\ S_L = \{i \in S : i \in S_k \text{ and } \mathbf{c}_i^{(1)} \in K_4\}, \\ S_L = \{i \in S : i \in S_k \text{ and } \mathbf{c}_i^{(1)} \in K_4\}, \\ S_L = \{i \in S : i \in S_k \text{ and } \mathbf{c}_i^{(1)} \in K_4\}, \\ S_L = \{i \in S : i \in S_k \text{ and } \mathbf{c}_i^{(1)} \in K_4\}, \\ S_L = \{i \in S : i \in S_k \text{ and } \mathbf{c}_i^{(1)} \in K_4\}, \\ S_L = \{i \in S : i \in S_k \text{ and } \mathbf{c}_i^{(1)} \in K_4\}, \\ S_L = \{i \in S : i \in S_k \text{ and } \mathbf{c}_i^{(1)} \in K_4\}, \\ S_L = \{i \in S_k \text{ and } \mathbf{c}_i^{(1)} \in K_4\}, \\ S_L = \{i \in S_k \text{ and } \mathbf{c}_i^{(1)} \in K_4\}, \\ S_L = \{i \in S_k \text{ and } \mathbf{c}_i^{(1)} \in K_4\}, \\ S_L = \{i \in S_k \text{ and } \mathbf{c}_i^{($	r6 boundary
	$S_L = \{i \in S : i \in S_k \text{ and } \mathbf{c}_i^* \in K_4\}$ $DC(r5/r6) = DC_{K_4}.$	
Step	DC = DC(r2/r3) + DC(r3/r4)	
6	+DC(r4/r5) + DC(r5/r6).	

https://doi.org/10.1371/journal.pcbi.1009077.t001

Supporting information

S1 Fig. Morphogen distributions. (A) The distribution of extracellular RA $[RA]_{out}$ at 14 hpf. **(B)** The distribution of free diffusible FGF, $[Fgf]_{free}$ at 14 hpf. **(C)** The A-P distribution of $[RA]_{out}$ in the morphogen domain and the higher magnification A-P distribution of $[RA]_{in}$ for the A-P range present in the responding tissue domain. The curves show the average morphogen level along the L-R axis. **(D)** The A-P distribution of free diffusible FGF, $[Fgf]_{signal}$ FGF signal, $[Fgf]_{signal}$. The curves show the average morphogen levels along the L-R axis. **(PDF)**

S2 Fig. Simulations with gene regulation alone with different convergence rates. (A-D) Time series of cell distributions with different convergence rates from 11–14 hpf. *hoxb1a* (red) and *krox20* (blue) expression. (A) Three simulations start with the same initial cell distribution (11 hpf) generated by the gene expression model. Cell distributions with (B) rapid, (C) medium and (D) slow initial convergence rates from 12–14 hpf. (E) The boundary sharpness index (SI) for four boundaries (SI(r2/r3), SI(r3/r4), SI(r4/r5) and SI(r5/r6)) and number of DC versus time. Histograms depicting three convergence rates analyzed for (F) rhombomere lengths of r3-5, (G) SI and (H) the number of DC. 100 independent stochastic simulations for each convergence rate based on the same parameters. Error bars represent standard deviation. (PDF)

S3 Fig. Timing of gene regulatory interactions influences hindbrain patterning. (A) Initial cell distribution at 11 hpf. (B-D) Time series of cell distributions with gene regulation limited to 1, 2 or 3 hour periods from 11–14 hpf while maintaining cell sorting throughout the simulations: (B) 11–12 hpf, (C) 11–13 hpf and (D) 11–14 hpf. All start with the same initial cell distribution and gene expression pattern. *hoxb1a* expression (red); *krox20* expression (blue). Dislocated cells (DCs) are highlighted by yellow edges. (E) The sharpness index (SI) for four boundaries (SI(r2/r3), SI(r3/r4), SI(r4/r5) and SI(r5/r6)) and number of DCs versus time. (F) Rhombomere lengths, (G) SIs and (H) DCs. 100 independent stochastic simulations for each type of convergence were computed under the same parameters. Error bars represent the standard deviation. (PDF)

S4 Fig. Timing of selective cell sorting influences hindbrain patterning. (A) Initial cell distributions at 11 hpf. (B-D) Time series of cell distributions with selective cell sorting during three different one-hour periods while maintaining gene regulation throughout the simulations: (B) 11–12 hpf, (C) 12–13 hpf and (D) 13–14 hpf. All three simulations start with the same initial cell distribution and gene expression pattern (11 hpf) generated by gene expression models. Selectivity is removed by setting the similarity function as a constant $\mathcal{F}=0.5$ such that cells sort randomly. hoxb1a expression (red), krox20 expression (blue). Dislocated cells (DCs) are highlighted by yellow edges. (E) Sharpness indices (SIs) and numbers of DCs (versus time. (F) Rhombomere lengths, (G) SIs and (H) DCs. 100 independent stochastic simulations for each type of convergence were computed under the same parameters. Error bars represent the standard deviation. (PDF)

S5 Fig. The relations between rhombomere length and the level of boundary sharpness (SI). Parameters for gene regulation are randomly perturbed and a total of n = 1000 simulations are displayed for each convergence rate. There are 513, 563 and 452 simulations for rapid, medium and slow convergence, respectively, that successfully generate the r2-6 pattern with four boundaries. Each point represents the corresponding quantities for each simulation.

(A-A") Length of r3 versus SI(r2/r3): (A) rapid, (A') medium and (A") slow convergence. (B-B") Length of r3 versus SI(r3/r4): (B) rapid, (B') medium and (B") slow convergence. (C-C") Length of r4 versus SI(r3/r4): (C) rapid, (C') medium and (C") slow convergence. (D-D") Length of r4 versus SI(r4/r5): (D) rapid, (D') medium and (D") slow convergence. (E-E") Length of r5 versus SI(r4/r5): (E) rapid, (E') medium and (E") slow convergence. (F-F") Length of r5 versus SI(r5/r6): (F) rapid, (F') medium and (F") slow convergence. (PDF)

S6 Fig. Additional information for the model. (A). Cell representation in SCEM: Each cell is represented by two layers of nodes and each layer has $N_{node} = 6$ nodes with a hexagonal structure. The pairwise lengths used in Eq (S9) have three possible constant values, l_{out} , l_{im} , l_{inter} . The length between two neighbor nodes in the outer layer is l_{out} . The length between two neighbor nodes in the inner layer is l_{im} . For two nodes in different layers with same angle, the length is l_{inter} . (B). An illustration of the distance function between cells and the boundary. For cells with identities belonging to the left side of the boundary (red cells), the proximal end is taken as the right-most edge of the cell. The distance is the Euclidean distance from the proximal edge to the boundary. Similarly, for the cell with identity belonging to the right side of the boundary (blue cells), the proximal edge is taken as the left-most edge of the cell. The distance is the Euclidean distance from the proximal edge to the boundary. For distances greater than 6^*r , (r is the radius of the cell), the cell is identified as a dislocated cell (DC). (C) The probability distribution for generating the initial distribution of cells in Fig 4B. There are five cell identities and each of them is a Gaussian with respect to A-P position. (PDF)

S7 Fig. Perturbations on mechanical model. The cell distributions at the end of the simulation (14hpf) are shown for the case with perturbed mechanical forces. (A) 10% reduction on attraction results in five-segment pattern with sharp boundaries. (B) 20% reduction on attraction results in completely separation and gaps between cells with different identities. Cells with same identities gather together to form clones. The model fails to mimic the pattern formations. (C) 20% reduction on repulsion results in five-segment pattern with mixture boundaries. (PDF)

S8 Fig. Simulations with multiplicative noise. (A) Time series of cell distribution with rapid initial convergence. (B-D) Comparisons of rapid early convergence, medium convergence and slow initial convergence. Statistics for (B) rhombomere lengths, (C) SIs and (D) DCs. 10 independent stochastic simulations for each type of convergence were computed under the same parameters. Error bars represent the standard deviation. (PDF)

S9 Fig. Simulations with cell proliferation and growth. (A) A illustration of how a cell divides. First, the division line is selected and cell elongates in the direction perpendicular to the division line. When the cell elongates to a certain length, it divides and separate into two daughter cells. Then the two daughter cells grow to normal cells size. (B) Time series of cell distribution with rapid initial convergence. (C) The number of cells over time (11-14hpf). The curve is from 10 independent simulations and error bar represent standard deviation. There are no cell divides during in 11–11.5 hpf because cells need 30 minutes to prepare for division (cell elongation) and there are no cells elongated before our initial simulation time 11hpf. (D-F) Comparisons of rapid early convergence, medium convergence and slow initial convergence. Statistics for (D) rhombomere lengths, (E) SIs and (F) DCs. 10 independent stochastic simulations for each type of convergence were computed under the same parameters. Error

bars represent the standard deviation. (PDF)

S10 Fig. Comparison for models with convergent extension (CE) and without convergent extension. (A) Time series of cell distribution with rapid initial convergence. (B-D) Comparisons for models without convergent extension and with convergent extension. Statistics for (B) rhombomere lengths, (C) SIs and (D) DCs. 100 independent stochastic simulations for each type of convergence were computed under the same parameters. Error bars represent the standard deviation. (PDF)

S11 Fig. Simulations for equations without advections on $[RA]_{in}$ and $[FGF]_{signal}$. (A) Time series of cell distribution with rapid initial convergence. (B-D) Comparisons of rapid early convergence, medium convergence and slow initial convergence. Statistics for (B) rhombomere lengths, (C) SIs and (D) DCs. 10 independent stochastic simulations for each type of convergence were computed under the same parameters. Error bars represent the standard deviation. (E-F) the A-P distribution of $[RA]_{out}$ in the morphogen domain and the higher magnification A-P distribution of $[RA]_{in}$ for the A-P range present in the tissue domain. The curves show the average morphogen level along the L-R axis. Cases with (E) or without (F) advections in $[RA]_{in}$ and $[FGF]_{signal}$. (PDF)

S1 Text. This file contains Supplementary Material including modeling details, parameter values, and experimental data.

(PDF)

Author Contributions

Conceptualization: Yuchi Qiu, Lianna Fung, Thomas F. Schilling, Qing Nie.

Data curation: Yuchi Qiu, Lianna Fung, Thomas F. Schilling, Qing Nie.

Formal analysis: Yuchi Qiu, Lianna Fung, Thomas F. Schilling, Qing Nie.

Funding acquisition: Thomas F. Schilling, Qing Nie.

Investigation: Yuchi Qiu, Lianna Fung, Thomas F. Schilling, Qing Nie.

Methodology: Yuchi Qiu, Lianna Fung, Thomas F. Schilling, Qing Nie.

Project administration: Thomas F. Schilling, Qing Nie.

Resources: Thomas F. Schilling, Qing Nie.

Software: Yuchi Qiu, Qing Nie.

Supervision: Thomas F. Schilling, Qing Nie.

Validation: Yuchi Qiu, Lianna Fung, Thomas F. Schilling, Qing Nie.

Visualization: Yuchi Qiu, Lianna Fung, Thomas F. Schilling, Qing Nie.

Writing - original draft: Yuchi Qiu, Lianna Fung, Thomas F. Schilling, Qing Nie.

Writing - review & editing: Yuchi Qiu, Lianna Fung, Thomas F. Schilling, Qing Nie.

References

- Lander AD. Pattern, growth, and control. Cell. 2011; 144(6):955–69. https://doi.org/10.1016/j.cell.2011. 03.009 PMID: 21414486
- Rogers KW, Schier AF. Morphogen gradients: from generation to interpretation. Annual review of cell and developmental biology. 2011; 27:377–407. https://doi.org/10.1146/annurev-cellbio-092910-154148 PMID: 21801015
- Towers M, Tickle C. Growing models of vertebrate limb development. Development. 2009; 136(2):179–90. https://doi.org/10.1242/dev.024158 PMID: 19103802
- Jaeger J, Surkova S, Blagov M, Janssens H, Kosman D, Kozlov KN, et al. Dynamic control of positional information in the early Drosophila embryo. Nature. 2004; 430(6997):368–71. https://doi.org/10.1038/ nature02678 PMID: 15254541
- Jaeger J. Modelling the Drosophila embryo. Molecular BioSystems. 2009; 5(12):1549–68. https://doi. org/10.1039/b904722k PMID: 20023719
- Hubaud A, Pourquié O. Signalling dynamics in vertebrate segmentation. Nature Reviews Molecular Cell Biology. 2014; 15(11):709–21. https://doi.org/10.1038/nrm3891. PMID: 25335437
- Yoshioka-Kobayashi K, Matsumiya M, Niino Y, Isomura A, Kori H, Miyawaki A, et al. Coupling delay controls synchronized oscillation in the segmentation clock. Nature. 2020; 580(7801):119–23. https://doi.org/10.1038/s41586-019-1882-z PMID: 31915376
- Baker RE, Schnell S, Maini PK. Mathematical models for somite formation. Current topics in developmental biology. 2008; 81:183–203. https://doi.org/10.1016/S0070-2153(07)81006-4 PMID: 18023728
- Fried P, Iber D. Dynamic scaling of morphogen gradients on growing domains. Nature communications. 2014; 5(1):1–12. https://doi.org/10.1038/ncomms6077 PMID: 25295831
- Ben-Zvi D, Pyrowolakis G, Barkai N, Shilo B-Z. Expansion-repression mechanism for scaling the Dpp activation gradient in Drosophila wing imaginal discs. Current biology. 2011; 21(16):1391–6. https://doi. org/10.1016/j.cub.2011.07.015 PMID: 21835621
- Zhu Y, Qiu Y, Chen W, Nie Q, Lander AD. Scaling a Dpp Morphogen Gradient through Feedback Control of Receptors and Co-receptors. Developmental Cell. 2020; 53(6):724–39. e14. https://doi.org/10.1016/j.devcel.2020.05.029 PMID: 32574592
- 12. Raspopovic J, Marcon L, Russo L, Sharpe J. Digit patterning is controlled by a Bmp-Sox9-Wnt Turing network modulated by morphogen gradients. Science. 2014; 345(6196):566–70. https://doi.org/10. 1126/science.1252960 PMID: 25082703
- Balaskas N, Ribeiro A, Panovska J, Dessaud E, Sasai N, Page KM, et al. Gene regulatory logic for reading the Sonic Hedgehog signaling gradient in the vertebrate neural tube. Cell. 2012; 148(1–2):273–84. https://doi.org/10.1016/j.cell.2011.10.047 PMID: 22265416
- 14. Zagorski M, Tabata Y, Brandenberg N, Lutolf MP, Tkačik G, Bollenbach T, et al. Decoding of position in the developing neural tube from antiparallel morphogen gradients. Science. 2017; 356(6345):1379–83. https://doi.org/10.1126/science.aam5887 PMID: 28663499
- Cohen M, Page KM, Perez-Carrasco R, Barnes CP, Briscoe J. A theoretical framework for the regulation of Shh morphogen-controlled gene expression. Development. 2014; 141(20):3868–78. https://doi.org/10.1242/dev.112573 PMID: 25294939
- Wang Q, Holmes WR, Sosnik J, Schilling T, Nie Q. Cell sorting and noise-induced cell plasticity coordinate to sharpen boundaries between gene expression domains. PLoS computational biology. 2017; 13 (1). https://doi.org/10.1371/journal.pcbi.1005307 PMID: 28135279
- Zhang L, Radtke K, Zheng L, Cai AQ, Schilling TF, Nie Q. Noise drives sharpening of gene expression boundaries in the zebrafish hindbrain. Molecular systems biology. 2012; 8(1). https://doi.org/10.1038/msb.2012.45 PMID: 23010996
- Bouchoucha YX, Reingruber J, Labalette C, Wassef MA, Thierion E, Dinh CDT, et al. Dissection of a Krox20 positive feedback loop driving cell fate choices in hindbrain patterning. Molecular systems biology. 2013; 9(1). https://doi.org/10.1038/msb.2013.46 PMID: 24061538
- 19. Meinecke L, Sharma PP, Du H, Zhang L, Nie Q, Schilling TF. Modeling craniofacial development reveals spatiotemporal constraints on robust patterning of the mandibular arch. PLoS computational biology. 2018; 14(11). https://doi.org/10.1371/journal.pcbi.1006569 PMID: 30481168
- 20. Du H, Wang Y, Haensel D, Lee B, Dai X, Nie Q. Multiscale modeling of layer formation in epidermis. PLoS computational biology. 2018; 14(2):e1006006. https://doi.org/10.1371/journal.pcbi.1006006 PMID: 29481568
- 21. Chou C-S, Lo W-C, Gokoffski KK, Zhang Y-T, Wan FY, Lander AD, et al. Spatial dynamics of multistage cell lineages in tissue stratification. Biophysical journal. 2010; 99(10):3145–54. https://doi.org/10.1016/j. bpj.2010.09.034 PMID: 21081061



- Wang Q, Oh JW, Lee H-L, Dhar A, Peng T, Ramos R, et al. A multi-scale model for hair follicles reveals heterogeneous domains driving rapid spatiotemporal hair growth patterning. Elife. 2017; 6. https://doi. org/10.7554/eLife.22772 PMID: 28695824
- 23. Nie Q, Qiao L, Qiu Y, Zhang L, Zhao W. Noise control and utility: From regulatory network to spatial patterning. Science China Mathematics. 2020:1–16.
- Qiao L, Zhao W, Tang C, Nie Q, Zhang L. Network Topologies That Can Achieve Dual Function of Adaptation and Noise Attenuation. Cell systems. 2019; 9(3):271–85. e7. https://doi.org/10.1016/j.cels. 2019.08.006 PMID: 31542414
- Lander A, Nie Q, Wan F. Membrane-associated non-receptors and morphogen gradients. Bulletin of mathematical biology. 2007; 69(1):33. https://doi.org/10.1007/s11538-006-9152-2 PMID: 17054000
- Shilo B-Z, Haskel-Ittah M, Ben-Zvi D, Schejter ED, Barkaj N. Creating gradients by morphogen shuttling. Trends in Genetics. 2013; 29(6):339–47. https://doi.org/10.1016/j.tig.2013.01.001 PMID: 23369355
- Lander AD, Lo W-C, Nie Q, Wan FY. The measure of success: constraints, objectives, and tradeoffs in morphogen-mediated patterning. Cold Spring Harbor Perspectives in Biology. 2009; 1(1):a002022. https://doi.org/10.1101/cshperspect.a002022 PMID: 20066078
- White RJ, Nie Q, Lander AD, Schilling TF. Complex regulation of cyp26a1 creates a robust retinoic acid gradient in the zebrafish embryo. PLoS biology. 2007; 5(11). https://doi.org/10.1371/journal.pbio. 0050304 PMID: 18031199
- 29. Eldar A, Rosin D, Shilo B-Z, Barkai N. Self-enhanced ligand degradation underlies robustness of morphogen gradients. Developmental cell. 2003; 5(4):635–46. https://doi.org/10.1016/s1534-5807(03) 00292-2 PMID: 14536064
- Sokolowski TR, Erdmann T, Ten Wolde PR. Mutual repression enhances the steepness and precision of gene expression boundaries. PLoS computational biology. 2012; 8(8). https://doi.org/10.1371/ journal.pcbi.1002654 PMID: 22956897
- 31. Rackauckas C, Schilling T, Nie Q. Mean-independent noise control of cell fates via intermediate states. iScience. 2018; 3:11–20. https://doi.org/10.1016/j.isci.2018.04.002 PMID: 30428314
- Exelby K, Herrera-Delgado E, Perez LG, Perez-Carrasco R, Sagner A, Metzis V, et al. Precision of tissue patterning is controlled by dynamical properties of gene regulatory networks. Development. 2021. https://doi.org/10.1242/dev.197566 PMID: 33547135
- Qiu Y, Chen W, Nie Q. Stochastic dynamics of cell lineage in tissue homeostasis. Discrete & Continuous Dynamical Systems-B. 2019; 24(8):3971. https://doi.org/10.3934/dcdsb.2018339 PMID: 32269502
- Schilling TF, Prince V, Ingham PW. Plasticity in zebrafish hox expression in the hindbrain and cranial neural crest. Developmental biology. 2001; 231(1):201–16. https://doi.org/10.1006/dbio.2000.9997 PMID: 11180963
- 35. Lumsden A, Krumlauf R. Patterning the vertebrate neuraxis. Science. 1996; 274(5290):1109–15. https://doi.org/10.1126/science.274.5290.1109 PMID: 8895453
- Wilkinson DG. Establishing sharp and homogeneous segments in the hindbrain. F1000Research. 2018; 7. https://doi.org/10.12688/f1000research.15391.1 PMID: 30135723
- Schilling TF, Nie Q, Lander AD. Dynamics and precision in retinoic acid morphogen gradients. Current opinion in genetics & development. 2012; 22(6):562–9. https://doi.org/10.1016/j.gde.2012.11.012
 PMID: 23266215
- Rhinn M, Dollé P. Retinoic acid signalling during development. Development. 2012; 139(5):843–58. https://doi.org/10.1242/dev.065938 PMID: 22318625
- 39. Maves L, Kimmel CB. Dynamic and sequential patterning of the zebrafish posterior hindbrain by retinoic acid. Developmental biology. 2005; 285(2):593–605. https://doi.org/10.1016/j.ydbio.2005.07.015 PMID: 16102743
- Sosnik J, Zheng L, Rackauckas CV, Digman M, Gratton E, Nie Q, et al. Noise modulation in retinoic acid signaling sharpens segmental boundaries of gene expression in the embryonic zebrafish hindbrain. Elife. 2016; 5:e14034. https://doi.org/10.7554/eLife.14034 PMID: 27067377
- Choe S-K, Zhang X, Hirsch N, Straubhaar J, Sagerström CG. A screen for hoxb1-regulated genes identifies ppp1r14al as a regulator of the rhombomere 4 Fgf-signaling center. Developmental biology. 2011; 358(2):356–67. https://doi.org/10.1016/j.ydbio.2011.05.676 PMID: 21787765
- **42.** Walshe J, Maroon H, McGonnell IM, Dickson C, Mason I. Establishment of hindbrain segmental identity requires signaling by FGF3 and FGF8. Current biology. 2002; 12(13):1117–23. https://doi.org/10.1016/s0960-9822(02)00899-0 PMID: 12121619
- Wiellette EL, Sive H. vhnf1 and Fgf signals synergize to specify rhombomere identity in the zebrafish hindbrain. Development. 2003; 130(16):3821–9. https://doi.org/10.1242/dev.00572 PMID: 12835397



- Labalette C, Wassef MA, Dinh CD-T, Bouchoucha YX, Le Men J, Charnay P, et al. Molecular dissection of segment formation in the developing hindbrain. Development. 2015; 142(1):185–95. https://doi.org/ 10.1242/dev.109652 PMID: 25516974
- **45.** Maves L, Jackman W, Kimmel CB. FGF3 and FGF8 mediate a rhombomere 4 signaling activity in the zebrafish hindbrain. Development. 2002; 129(16):3825–37. PMID: 12135921
- 46. Alexander T, Nolte C, Krumlauf R. Hox genes and segmentation of the hindbrain and axial skeleton. Annual Review of Cell and Developmental. 2009; 25:431–56. https://doi.org/10.1146/annurev.cellbio.042308.113423 PMID: 19575673
- 47. Parker HJ, Krumlauf R. Segmental arithmetic: summing up the Hox gene regulatory network for hind-brain development in chordates. Wiley Interdisciplinary Reviews: Developmental Biology. 2017; 6(6): e286. https://doi.org/10.1002/wdev.286 PMID: 28771970
- 48. Lecaudey V, Anselme I, Rosa F, Schneider-Maunoury S. The zebrafish Iroquois gene iro7 positions the r4/r5 boundary and controls neurogenesis in the rostral hindbrain. Development. 2004; 131(13):3121–31. https://doi.org/10.1242/dev.01190 PMID: 15175248
- 49. Addison M, Xu Q, Cayuso J, Wilkinson DG. Cell identity switching regulated by retinoic acid signaling maintains homogeneous segments in the hindbrain. Developmental cell. 2018; 45(5):606–20. e3. https://doi.org/10.1016/j.devcel.2018.04.003 PMID: 29731343
- Cooke JE, Kemp HA, Moens CB. EphA4 is required for cell adhesion and rhombomere-boundary formation in the zebrafish. Current Biology. 2005; 15(6):536–42. https://doi.org/10.1016/j.cub.2005.02.019 PMID: 15797022
- Xu Q, Mellitzer G, Robinson V, Wilkinson DG. In vivo cell sorting in complementary segmental domains mediated by Eph receptors and ephrins. Nature. 1999; 399(6733):267–71. https://doi.org/10.1038/20452 PMID: 10353250
- 52. Hernandez RE, Rikhof HA, Bachmann R, Moens CB. vhnf1 integrates global RA patterning and local FGF signals to direct posterior hindbrain development in zebrafish. Development. 2004; 131(18):4511–20. https://doi.org/10.1242/dev.01297 PMID: 15342476
- Pitulescu ME, Adams RH. Eph/ephrin molecules—a hub for signaling and endocytosis. Genes & development. 2010; 24(22):2480–92. https://doi.org/10.1101/gad.1973910 PMID: 21078817
- 54. Warga RM, Kimmel CB. Cell movements during epiboly and gastrulation in zebrafish. Development. 1990; 108(4):569–80. PMID: 2387236
- 55. Waskiewicz AJ, Rikhof HA, Moens CB. Eliminating zebrafish pbx proteins reveals a hindbrain ground state. Developmental cell. 2002; 3(5):723–33. https://doi.org/10.1016/s1534-5807(02)00319-2 PMID: 12431378
- Newman T. Modeling Multicellular Systems Using Subcellular Elements. Mathematical Biosciences & Engineering. 2(3):613. https://doi.org/10.3934/mbe.2005.2.613 PMID: 20369943
- 57. Theil T, Frain M, Gilardi-Hebenstreit P, Flenniken A, Charnay P, Wilkinson DG. Segmental expression of the EphA4 (Sek-1) receptor tyrosine kinase in the hindbrain is under direct transcriptional control of Krox-20. Development. 1998; 125(3):443–52. PMID: 9425139
- Papan C, Campos-Ortega JA. On the formation of the neural keel and neural tube in the zebrafishDanio (Brachydanio) rerio. Roux's archives of developmental biology. 1994; 203(4):178–86. https://doi.org/10. 1007/BF00636333 PMID: 28305881
- 59. Huebner RJ, Wallingford JB. Coming to consensus: a unifying model emerges for convergent extension. Developmental cell. 2018; 46(4):389–96. https://doi.org/10.1016/j.devcel.2018.08.003 PMID: 30130529
- Shindo A. Models of convergent extension during morphogenesis. Wiley Interdisciplinary Reviews: Developmental Biology. 2018; 7(1):e293.
- **61.** Sutherland A, Keller R, Lesko A, editors. Convergent extension in mammalian morphogenesis. Seminars in cell & developmental biology; 2020: Elsevier.
- Keller R, Tibbetts P. Mediolateral cell intercalation in the dorsal, axial mesoderm of Xenopus laevis. Developmental biology. 1989; 131(2):539–49. https://doi.org/10.1016/s0012-1606(89)80024-7 PMID: 2463948
- 63. Ahrens MJ, Li Y, Jiang H, Dudley AT. Convergent extension movements in growth plate chondrocytes require gpi-anchored cell surface proteins. Development. 2009; 136(20):3463–74. https://doi.org/10.1242/dev.040592 PMID: 19762422
- **64.** Kimmel CB, Miller CT, Kruze G, Ullmann B, BreMiller RA, Larison KD, et al. The shaping of pharyngeal cartilages during early development of the zebrafish. Developmental biology. 1998; 203(2):245–63. https://doi.org/10.1006/dbio.1998.9016 PMID: 9808777
- Barrow JR, Stadler HS, Capecchi MR. Roles of Hoxa1 and Hoxa2 in patterning the early hindbrain of the mouse. Development. 2000; 127(5):933–44. PMID: 10662633



- 66. Reifers F, Bohli H, Walsh EC, Crossley PH, Stainier D, Brand M. Fgf8 is mutated in zebrafish acerebellar (ace) mutants and is required for maintenance of midbrain-hindbrain boundary development and somitogenesis. Development. 1998; 125(13):2381–95. PMID: 9609821
- 67. Häärä O, Harjunmaa E, Lindfors PH, Huh S-H, Fliniaux I, Åberg T, et al. Ectodysplasin regulates activator-inhibitor balance in murine tooth development through Fgf20 signaling. Development. 2012; 139 (17):3189–99. https://doi.org/10.1242/dev.079558 PMID: 22833125
- Nacu E, Gromberg E, Oliveira CR, Drechsel D, Tanaka EM. FGF8 and SHH substitute for anterior–posterior tissue interactions to induce limb regeneration. Nature. 2016; 533(7603):407–10. https://doi.org/10.1038/nature17972 PMID: 27120163
- Müller P, Rogers KW, Jordan BM, Lee JS, Robson D, Ramanathan S, et al. Differential diffusivity of Nodal and Lefty underlies a reaction-diffusion patterning system. Science. 2012; 336(6082):721–4. https://doi.org/10.1126/science.1221920 PMID: 22499809
- Shen MM. Nodal signaling: developmental roles and regulation. Development. 2007; 134(6):1023–34. https://doi.org/10.1242/dev.000166 PMID: 17287255
- Briscoe J, Small S. Morphogen rules: design principles of gradient-mediated embryo patterning. Development. 2015; 142(23):3996–4009. https://doi.org/10.1242/dev.129452 PMID: 26628090
- Liem K, Jessell TM, Briscoe J. Regulation of the neural patterning activity of sonic hedgehog by secreted BMP inhibitors expressed by notochord and somites. Development. 2000; 127(22):4855–66. PMID: 11044400
- 73. García-García MJ, Shibata M, Anderson KV. Chato, a KRAB zinc-finger protein, regulates convergent extension in the mouse embryo. Development. 2008; 135(18):3053–62. https://doi.org/10.1242/dev. 022897 PMID: 18701545
- 74. Fulton T, Trivedi V, Attardi A, Anlas K, Dingare C, Arias AM, et al. Axis Specification in Zebrafish Is Robust to Cell Mixing and Reveals a Regulation of Pattern Formation by Morphogenesis. Current Biology. 2020; 30(15):2984–94. e3. https://doi.org/10.1016/j.cub.2020.05.048 PMID: 32559447
- 75. Čanić S. Moving boundary problems. Bulletin of the American Mathematical Society. 2021; 58(1):79–106.
- 76. Kulesa PM, Fraser SE. Segmentation of the vertebrate hindbrain: a time-lapse analysis. International Journal of Developmental Biology. 1998; 42(3):385–92. PMID: 9654023
- 77. Thierion E, Le Men J, Collombet S, Hernandez C, Coulpier F, Torbey P, et al. Krox20 hindbrain regulation incorporates multiple modes of cooperation between cis-acting elements. PLoS genetics. 2017; 13 (7):e1006903. https://doi.org/10.1371/journal.pgen.1006903 PMID: 28749941
- Buckles GR, Thorpe CJ, Ramel M-C, Lekven AC. Combinatorial Wnt control of zebrafish midbrain– hindbrain boundary formation. Mechanisms of development. 2004; 121(5):437–47. https://doi.org/10. 1016/j.mod.2004.03.026 PMID: 15147762
- Kimmel CB, Ballard WW, Kimmel SR, Ullmann B, Schilling TF. Stages of embryonic development of the zebrafish. Developmental dynamics. 1995; 203(3):253–310. https://doi.org/10.1002/aja.1002030302 PMID: 8589427
- 80. Thisse C, Thisse B, Schilling T, Postlethwait J. Structure of the zebrafish snail1 gene and its expression in wild-type, spadetail and no tail mutant embryos. Development. 1993; 119(4):1203–15. PMID: 8306883
- Begemann G, Schilling TF, Rauch G-J, Geisler R, Ingham PW. The zebrafish neckless mutation reveals a requirement for raidh2 in mesodermal signals that pattern the hindbrain. Development. 2001; 128 (16):3081–94. PMID: 11688558
- Oxtoby E, Jowett T. Cloning of the zebrafish krox-20 gene (krx-20) and its expression during hindbrain development. Nucleic acids research. 1993; 21(5):1087–95. https://doi.org/10.1093/nar/21.5.1087
 PMID: 8464695
- **83.** Mercier P, Simeone A, Cotelli F, Boncinelli E. Expression pattern of two otx genes suggests a role in specifying anterior body structures in zebrafish. International Journal of Developmental Biology. 2004; 39(4):559–73.
- 84. Cheng CN, Li Y, Marra AN, Verdun V, Wingert RA. Flat mount preparation for observation and analysis of zebrafish embryo specimens stained by whole mount in situ hybridization. JoVE (Journal of Visualized Experiments). 2014;(89):e51604. https://doi.org/10.3791/51604 PMID: 25078510
- 85. Schumacher LJ, Kulesa PM, McLennan R, Baker RE, Maini PK. Multidisciplinary approaches to understanding collective cell migration in developmental biology. Open biology. 2016; 6(6):160056. https://doi.org/10.1098/rsob.160056 PMID: 27278647
- 86. Rørth P. Fellow travellers: emergent properties of collective cell migration. EMBO reports. 2012; 13 (11):984–91. https://doi.org/10.1038/embor.2012.149 PMID: 23059978

